Nuclear Physics B75 (1974) 189–245. North-Holland Publishing Company

HIGH STATISTICS STUDY OF THE REACTION $\pi^- p \to \pi^- \pi^+ n$: APPARATUS, METHOD OF ANALYSIS, AND GENERAL FEATURES OF RESULTS AT 17 GeV/c

G. GRAYER*, B. HYAMS, C. JONES, P. SCHLEIN** and P. WEILHAMMER
CERN, Geneva, Switzerland

W. BLUM, H. DIETL, W. KOCH ***, E. LORENZ, G. LÜTJENS, W. MÄNNER, J. MEISSBURGER, W. OCHS and U. STIERLIN
Max-Planck-Institute für Physik und Astrophysik, Munich, Germany

Received 31 December 1973

Abstract: A detailed account is given of a high statistics experiment measuring the reaction $\pi^- p \to \pi^- \pi^+ n$ at 17.2 GeV/c. The spark chamber and counter triggering system are desribed. The methods of data analysis are described, in particular the determination of angular distributions from apparatus with limited acceptance. Experimental data and their interpretation are presented.

1. Introduction

Using a wire chamber spectrometer installed at CERN during 1970–1971 we have investigated various quasi two-body reactions with high event statistics, recording a total of 12×10^6 triggers. Some results of these measurements have already been reported elsewhere [1–13].

In this paper we present a study of the reaction

$$\pi^- p \to \pi^+ \pi^- n \qquad (1)$$

at 17.2 GeV/c beam momentum which has been performed with just over 300 000 reconstructed events, the largest data sample of a specific reaction analysed with our apparatus. The performance of the spectrometer and the analysis procedures applied, as explicitly described in this study, are representative of the experimental methods we have employed for all reactions measured in our set-up.

In this experiment the momenta of the secondary pions were measured, and the undetected neutron was identified by calculating the missing mass. With this tech-

* Now at Max-Planck-Institute, Munich
** Permanent adress: University of California, Los Angeles.
*** Now at DESY, Hamburg.

nique the detection efficiency is insensitive to the proton-neutron four-momentum transfer t in the range $0 < |t| \lesssim 0.6\ (\mathrm{GeV}/c)^2$, unlike an experiment which detects the neutron and necessarily has zero efficiency at $t = 0$.

Reaction (1) has previously been studied for many years in many experiments [14- 17]. However, the very fact that the knowledge about this reaction had reached a certain level of theoretical understanding demanded experiments with high statistics which could decide on specific theoretical questions.

The main interest in this reaction lies in the study of the $\pi^+\pi^-$ system, its resonant states or more generally $\pi\pi$ phase shifts, and in the investigation of the production mechanism with its various aspects of particle (trajectory) exchanges and absorption effects. Especially for the $\pi\pi$ phase-shift analysis, high event statistics are a necessity if one is to decide between ambiguities in phase-shift solutions. Similarly, for investigating the vector-dominance relations between ρ^0 production in reaction (1) and π photoproduction, high statistics are indispensable.

In sects. 2 and 3 of this paper we give a description of the spectrometer and our method of analysis. Sect. 4 shows the general experimental results on reaction (1) such as differential cross sections, spherical harmonic moments of the $\pi^+\pi^-$ angular distribution, resonance parameters for the observed ρ, f and g mesons, and $\pi\pi$ phase shifts. A more detailed treatment of these topics, and comparison of the results with theoretical models, have been and will be treated elsewhere [4,5,8,10].

2. Apparatus

The apparatus we used was a single-arm spectrometer for the measurement of fast forward-going particles (fig. 1). It consisted of a 50 cm long liquid-hydrogen target H_2, three sets of spark chambers (W_1, W_2, W_3), an analysing magnet M, and scintillation and Čerenkov counters for trigger selection and particle identification. The following convention is used for the coordinate system: the z-axis is defined by the direction of the incoming beam, x denotes the horizontal axis, and y the vertical axis.

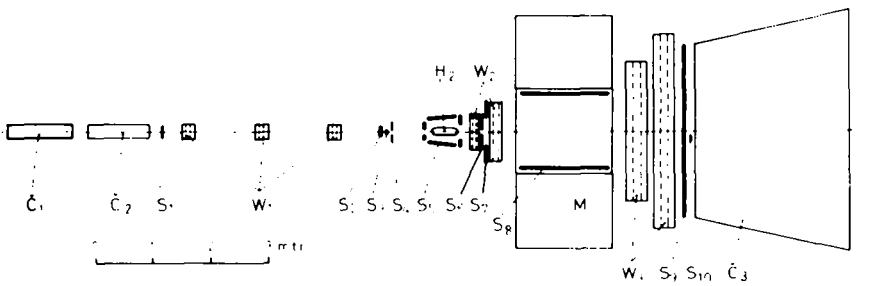

Fig. 1. Apparatus. Details are described in text.

2.1. Beam

The experiment used an unseparated negative beam, produced in a 6 × 6 × 120 mm^3 tungsten target in a slow ejected proton beam. The production angle was 22 mrad. Pions up to a momentum of 18.8 GeV/c could be obtained. The particles were focused with a quadrupole doublet on to an adjustable momentum slit and then refocused on to the hydrogen target through a triplet of quadrupoles. Two bending magnets before and after the intermediate focus deflected the beam from the primary proton line by 250 mrad. The beam was not corrected for chromatic dispersion. At the second focus the measured value of the dispersion was 8.5 mm for $\Delta p/p = 1\%$. The beam intensity was regulated with a collimator to about 60 000 pions per burst of 300 msec. Due to a beam-defining anticoincidence counter and a pile-up rejection system, the effective beam was 35 000 particles per burst. For this intensity and for 17.2 GeV/c beam momentum the spread was ±0.75%.

The horizontal and vertical dimensions of the beam were $\Delta x = 7$ mm and $\Delta y = 8$ mm at the position of the hydrogen target. The beam divergences were $\Delta\theta_x = 8.7$ mrad and $\Delta\theta_y = 3.0$ mrad (Δx, Δy, $\Delta\theta_x$, $\Delta\theta_y$ = full width at half maximum).

The beam contained a background of (2.4 ± 0.5)% muons, (0.4 ± 0.05)% kaons, less than 0.4% electrons, and about 0.04% antiprotons. Kaons and antiprotons were tagged by two beam Cerenkov counters C1, C2 filled with CO_2 at 0.3 atm pressure and propane at 1.2 atm pressure, respectively.

2.2. Spark chambers

Fig. 1 shows the position of the wire spark chambers. The first set W_1, in front of the target, was used to measure the direction of the incident beam. The direction of the charged secondary particles was measured in the set W_2. The third set W_3 was used to measure the deflections of these particles in order to determine their momenta.

Table 1
Essential parameters of the spark chambers

Chamber set		1	2		3	
			A	B	A	B
Number in set		12	6	6	6	6
Sensitivity area (m^2)		0.25 × 0.25	0.7 × 0.7	1.0 × 0.4	2.6 × 0.9	3.6 × 0.9
Wire orientation[a]		0, +45°, −45°, 90°	0, +45°, −45°, 90°	0, +45°, −45°, 90°	0, +30°, −30°	0, +30°, −30°
Average resolution (mm)	Pos. plane	0.14	0.20	0.25	0.25	0.25
	Neg. plane	0.21	0.27	0.32	0.32	0.32

a) ...

The chambers had magnetostrictive read-out on both planes. Wire spacing was 1 mm and the gap width 10 mm. Owing to the recharging time of the high-voltage system, the maximum trigger rate was limited to one trigger per 15 msec. Further details on the sensitive area, the wire orientation, and the resolution are listed in table1. The construction and performance of the biggest chambers have been de scribed elsewhere [7].

The spark chambers were aligned mechanically to an accuracy of better than ±0.5 mm. The exact x and y position of each chamber was then determined by a program fitting straight tracks which traversed all chambers. During the experiment this was done twice a day.

2.3. Spectrometer magnet

The window-frame-type magnet had a gap of 150 × 110 × 50 cm^3 (width × length × height). The bending power was $2T \cdot m$; thus particles with a momentum below 600 MeV/c did not traverse the apparatus. Iron plates on both sides of the magnet shielded the read-out system of the spark chambers from the magnet stray field.

The field components were measured at 30 000 points to an accuracy of 0.3% of the main component [18]. During the experiment the stability of the magnetic field was monitored to better than 0.2%.

2.4. Čerenkov counter for identification of secondary particles

The secondary particles were identified by a threshold gas Čerenkov counter $\check{C}_3$ operating at atmospheric pressure. Having lateral dimensions of 420 × 140 cm^2 at the downstream end, the counter accepted all particles passing the magnet gap with momenta above 5 GeV/c. The radiator length was 270 ± 10 cm. The counter consisted of 14 cells with spherically figured mirrors, which reflected the light onto 5″ diameter photomultipliers mounted above and below the sensitive area. At 17.2 GeV/c primary momentum the counter was filled with CO_2 ($n = 1.00042$). Fig. 2 shows the pion detection inefficiency as a function of momentum. The main source for the small inefficiency above 6 GeV/c momentum comes from undetected interactions of pions in the counter hodoscope in front of the Cerenkov counter and in the 1mm thick front window. A more detailed description of this counter will be given elsewhere.

The counter was not included in the trigger selection, but the signal pattern of the 14 photomultipliers was recorded on magnetic tape, together with the spark coordinates.

2.5. Counters and trigger logic

The trigger selection was performed with the scintillation counters $S_1, \ldots, S_{10}$, whose dimensions are listed in table 2.

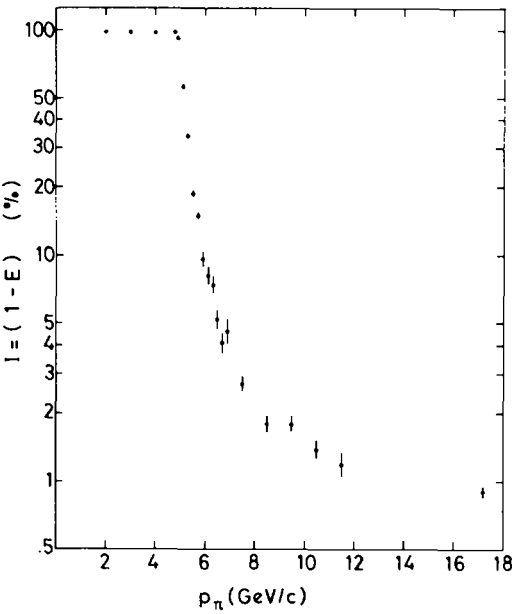

Fig. 2. Inefficiency (= 1 – efficiency) of gas Čerenkov counter $\check{C}_3$ for pions as a function of pion momentum.

Table 2
Essential parameters of scintillation counters

Counter	Scintillator thickness per layer (mm)	Layers of scintillator	Layers of lead	Maximum width (cm)	Maximum height (cm)	Other features
S_1	2	1		14	10	
S_2	2	1		10	10	
S_3	2	1		3	3	
S_4	10	1		30	30	25 mm ϕ central hole
$S_{5.1}$, $S_{5.3}$	5	1				Shown in fig. 2
$S_{5.2}$	5	5	4			Round 32 cm ϕ, 4 cm hole
$S_{5.4} \ldots S_{5.13}$	5	6	6	35	70	
S_6	2	1		50	40	Variable central hole ~25 × 40mm^2
S_7	5	5	4	120	50	
$S_{8.1} \ldots S_{8.10}$	5	2	1	75	120	
S_9	5	2		10	100	Two fences of 32 scintillators
S_{10}	5	2		14	6	Consisted of two counters with adjustable overlap

The incoming beam was defined by the coincidence of the counters S_1, S_2, S_3. The counters S_1 and S_2 were large enough to monitor also the beam halo. The anti-coincidence counter S_4 in front of the target with a central hole of 25 mm defined the accepted beam. Interactions were detected by the counter system S_6 which allowed the non-interacting beam to pass through a rectangular hole matched in size to the hole in S_4. The final selection of reactions with a definite number of charged secondary particles was made with the counter array S_9. The array consisted of two rows of 32 counters mounted pairwise. Each pair was connected to a twofold coincidence, thus reducing accidental triggers.

Only a small fraction of π^- p interactions involve the production of two forward going charged particles and a neutron. Since in this experiment the neutron was not detected, a very efficient counter system was necessary to suppress other reactions, especially those invoving a slow π^0 and hence not readily distinguished by a missing-mass calculation. Except for a hole for the incoming beam and a window for forward-going particles, the target was completely surrounded by two layers of anti-coincidence counters $S_{5.1}$, ..., $S_{5.13}$. The arrangement of the counters is shown in fig. 3. The counters $S_{5.1}$, $S_{5.2}$, and $S_{5.3}$ were mounted inside the vacuum vessel of the target, vetoing events with slow charged particles leaving the target sideways or backwards. Furthermore, lead scintillator sandwich counters $S_{5.4}$, ..., $S_{5.13}$, each having a total of four conversion length for γ-rays, were arranged around the target vessel to detect reactions with π^0 production. The lead scintillator sandwich veto counters S_7 in front of the magnet and S_8 on the magnet gap faces further improved the trigger selection.

An example of the selectivity of the anticoincidence counters around the target is shown in figs. 4a and 4b. Fig. 4a shows the missing mass distribution for a sample of two-prong events (where at least one particle produced a signal in the gas Čerenkov counter) when only the anticoincidence counters S_7 and S_8 were included in the trigger. The signals of the counters $S_{5.1}$, ..., $S_{5.13}$ were recorded together with the spark coordinates on tape. Besides a peak at the neutron mass we observe a significant

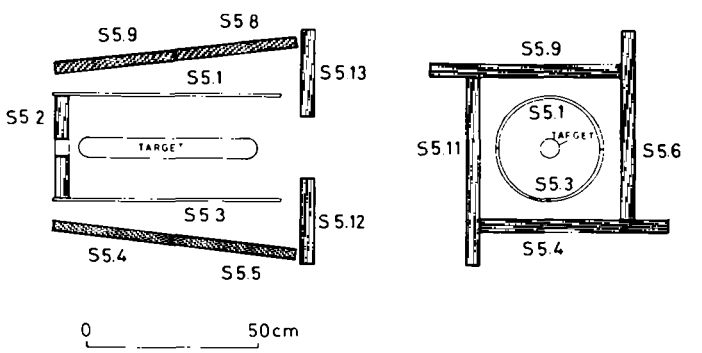

Fig. 3. Arrangement of anticoincidence counters around target.

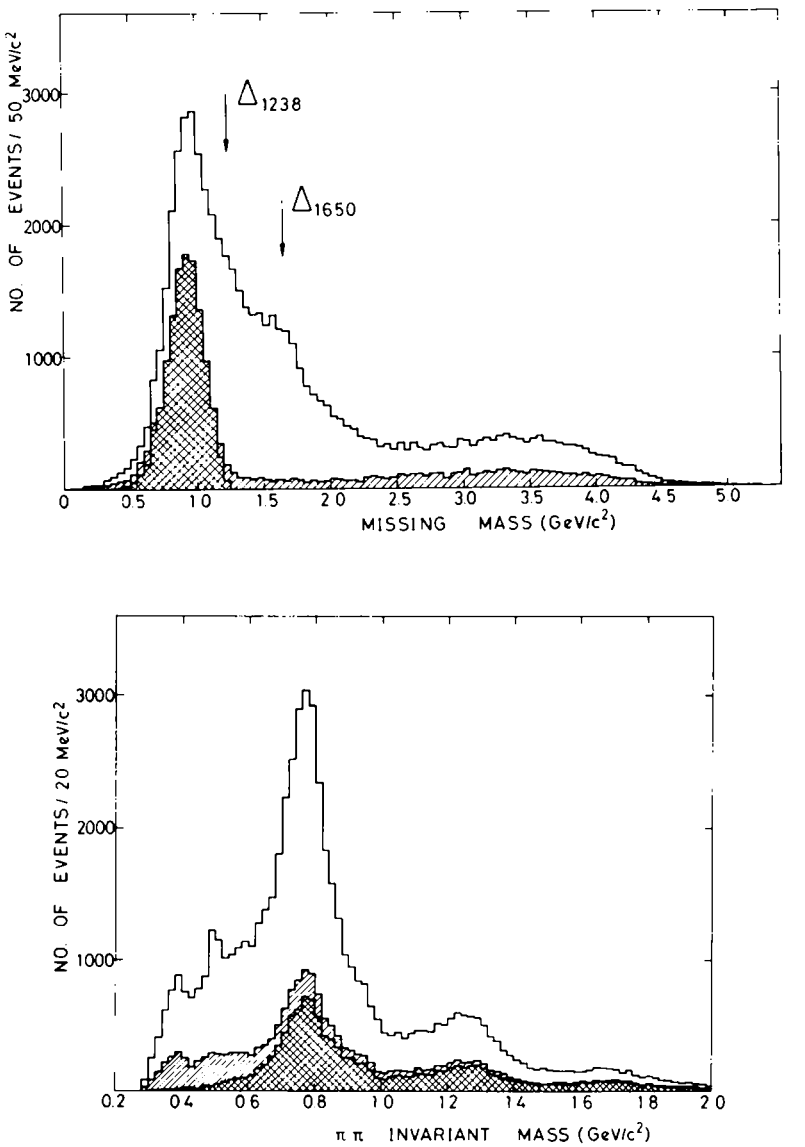

Fig. 4. (a) Missing mass distribution for $\pi^- p \to \pi^+ \pi^- MM$ for different types of trigger selection. (b) $\pi^+ \pi^-$ invariant mass spectrum for different types of trigger selection: ⬚ anticoincidence counters not used around target, ▨ anticoincidence counters used around target, ▩ selection of events with a missing neutron.

contribution of $\Delta(1236)$ and $\Delta(1650)$. The hatched area shown the missing-mass distribution for events with no signal from the counters around the target. Besides the peak at the neutron mass, a contribution of events with high missing mass is observed. These are mainly events where some π^0's escape the anticoincidence counter system in the forward direction. The significant difference of $\sim 35\%$ between the spectra at the neutron position shows the losses caused by δ-electrons and neutrons detected by the counters. Also indicated is the missing-mass distribution for events that fulfilled our χ^2 selection criteria for a neutron.

Fig. 4b shows the corresponding invariant mass spectra.

One of the main sources of unwanted triggers was non-interacting (or elestically scattered) beam producing a signal in S_6, and two signals in the counter array from the beam particle and a knock-on electron. Most of these triggers were suppressed by a small anticoincidence counter system S_{10} mounted behind the counter array S_9 on the beam trajectory.

The final trigger condition was:

(a) a beam particle entering the hydrogen target $\equiv (S_1 \cdot S_2 \cdot S_3 \cdot S_4)$;

(b) an interaction in the target $\equiv (S_6)$;

(c) observation of two, and only two, signals in the counter array $\equiv (S_9)_2$;

(d) no signal in the anticoincidence counters $\equiv (S_{5\cdot1} \ldots\ldots S_{5\cdot13} \cdot S_7 \cdot S_8 \cdot S_{10})$.

The trigger selection gave one trigger for 4 400 incoming beam particles, which corresponds to 1 trigger for 200 interactions or a triggered cross section of 130 μb.

The recorded data comprised:

21% "good" events (two-prong events with opposite charge with a missing-mass MM in the range $0.50\ \mathrm{GeV}/c^2 < MM < 1.23\ \mathrm{GeV}/c^2$);

19% inelastic events (mainly associated with one or more π^0's escaping from the target in the forward direction):

3% two-prong events where both particles had the same charge;

31% beam particles associated with δ-electrons;

10% three-prong events (mainly events where two particles pass one array counter or one track passes a gap between two array counters);

7% interactions of beam particles after the target;

9% of the triggers had an extra track in the beam chambers. We did not process or classify further this category of event.

In order to make efficient use of the apparatus, we often triggered not only with the selection described above but also with some other logic, selecting another reaction using separate chains of coincidence circuits. For example, the reaction [1] $\pi^- p \to A_2 p \to K^- K^0 p$ and a calibration of the neutron sensitivity of the anticoincidence counters around the target were recorded together with the reaction $\pi^- p \to \pi^+ \pi^- n$. Owing to spark gap recharging and data transfer time, we had about 60% duty cycle during the burst for triggering on these three reactions in parallel.

2.6. Computer control

A DEC PDP-9 computer was used to control the data acquisition and storage on magnetic tape.

For each event we recorded information both from the magnetostrictive chambers and from the fast electronics. The magnetostricitve signals were digitized in a SEN SPADAC system of 448 binary 16-bits scalers using a 30MHz clock. Signals from the triggering counters and coincidence units were recorded in an 80-bit pattern unit. Additional data such as the contents of fast scalers were recorded at intervals of 15 minutes.

The event data were edited before they were written on mgnetic tape and this procedure (as well as the previously mentioned spark gap recharging time) limited our data-taking rate to approximately 15 msec per event.

When not occupied with the main program outlined above, the computer executed a background program which examined about 10% of the data in order to recognize malfunction of the spark chambers, trigger electronics, and data editing. The program produced on a storage oscilloscope a comprehensive display of spark positions, tracks from pattern recognition, and counter information. This proved itself to be a powerful monitor of the quality of the data being recorded.

3. Data analysis

3.1. Geometric reconstruction and kinematic analysis of events

The events were processed off line on IBM 360/91 and CDC 6600 computers.

As a first step, sparks were sorted for each set of spark chambers into straight line segments independently in two projections. The other projections were then used to combine the two segments.

All points found to belong to the line segments entered into a geometric fit, constraining the tracks to form a vertex and constructing trajectories through the magnet with a stepwise integration. From this fit we obtained the momentum vectors of the charged secondaries. Finally, a kinematic fit to the event hypothesis was performed.

Losses of good events through the reconstruction program were determined by scanning by eye storage oscilloscope display of some 6 000 triggers corresponding to some 1 200 good events. We found the loss to be less than 4%. In addition to this there was a chance of $\leqslant 1\%$ that a good two-prong event, recorded with an accompanying beam track, was wrongly identified as a three-prong event and was therefore lost.

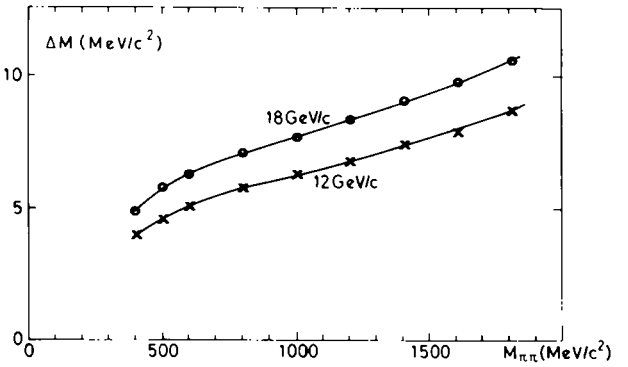

Fig. 5. $\pi\pi$ invariant mass resolution $\Delta M_{\pi\pi}$ (= standard deviation) as a function of $M_{\pi\pi}$ for $\pi\pi$ energies of 12 and 18 GeV.

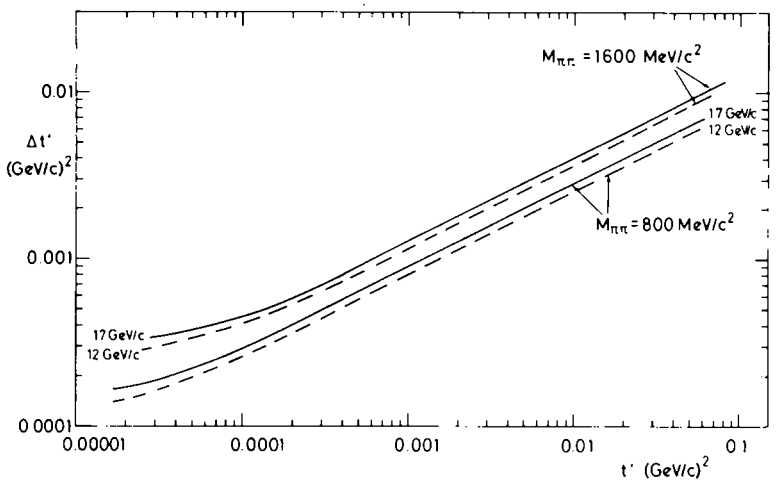

Fig. 6. Experimental error in $t' = t - t_{min}$ as a function of t' for the reaction $\pi^- p \to \pi^+ \pi^- n$ at beam momenta of 12 and 18 GeV/c. The two upper lines refer to an invariant $\pi\pi$ mass of 1 600 MeV/c^2, the lower lines to a mass of 800 MeV/c^2.

3.2. Measurement accuracy

The spectrometer resolution for the invariant mass of $\pi^+ \pi^-$ pairs is determined by multiple scattering in the H_2 target and chambers, and by errors in measuring angles. Measuring and multiple scattering errors contribute equally to the invariant mass resolution at around 15 GeV pair energy. Fig. 5 shows the calculated π pair invariant mass resolution as a function of invariant mass for pairs of 12 GeV and 18 GeV total energy. The calculation is based on observed values of chamber measurement errors [7] and calculated values of the multiple scattering in the spectrom-

eter. It agrees to within 10% with the observed width of the K^0, our only adequate calibration signal [1]. The central value we observed for the K^0 mass was 498.6 MeV/c^2.

Scattering and measuring errors give comparable contributions to the errors in determining the fitted squared four-momentum transfer t (from proton to neutron). Fig. 6 shows $\Delta t' = \Delta(t - t_{min})$ as a function of t', $M_{\pi\pi}$, and beam energy.

The missing-mass resolution was dominated by the uncertainty in the incident π beam energy and the error of measurement of the momentum of the faster outgoing pion. It had a standard deviation of around 200 MeV/c^2 for π-pair data recorded with a 17 GeV/c π beam.

3.3. Corrections for detection inefficiencies

Some fraction of produced events that would have been accepted by the geometry of the set-up was not observed because of various detection inefficiencies. In the following subsections we discuss those inefficiencies which depend on the event geometry and kinematics and were corrected event by event. The correction was performed by introducing for every event i an individual weight w_i which was calculated as the product of all weight factors $w_i^{(\alpha)}$ arising from inefficiencies of type α. The weight distribution had an average of $\langle w \rangle = 1.48$ with the extremes 1.15 and 2.10.

3.3.1. Secondary interactions in the target

The correction due to secondary particle interactions in the target was calculated from the path length of the secondaries and their total cross section in hydrogen. The mean correction factor was $\langle w^{(t)} \rangle = 1.05$.

3.3.2. δ-rays triggering the anticoincidence counters inside the target vessel

This loss was measured by triggering on $\pi^+ \pi^-$ n events with the additional condition that one of the counters $S_{5\cdot1}$ or $S_{5\cdot3}$ (inside the vacuum tank) should give a signal. The events lost in the normal trigger were selected by a neutron missing-mass criterion. It was found that the fraction of events lost dependend only on the vertex position. Fig. 7 shows the measured correction function. Although the δ-ray loss with $\langle w^{(\delta)} \rangle = 1.25$ gives the biggest contribution to the weights, its influence on the shape of the differential cross sections is rather small, because it enters only through the vertex dependence of the geometric acceptance.

3.3.3. Neutrons detected by the veto counters

The anticoincidence counters around the target caused a certain loss of wanted events by veto signals from neutrons interacting in the scintillator. A sketch of the target region is seen in fig. 3, with the cylindrical scintillation counters $S_{5\cdot1}$ and $S_{5\cdot3}$, and the eight plane lead-sandwich counters $S_{5\cdot4}$, ..., $S_{5\cdot13}$.

During part of the experiment "neutron loss" events were recorded, requiring

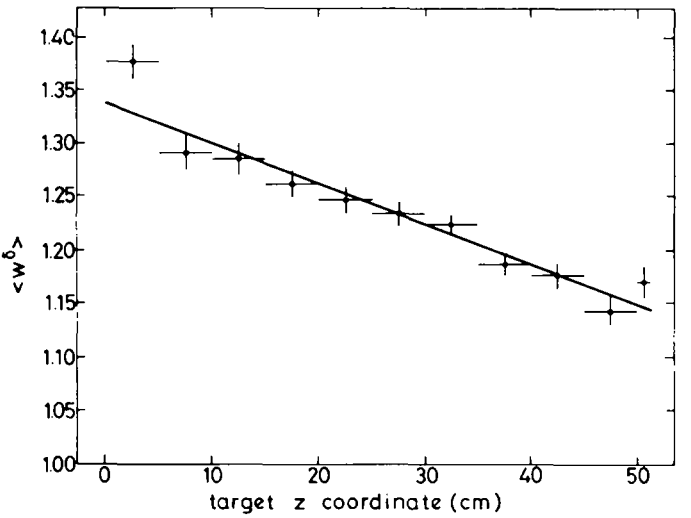

Fig. 7. Weight factor correcting for events which were lost due to δ-ray signals in inner target counters. The weight is plotted as a function of the distance between interaction point and target entrance.

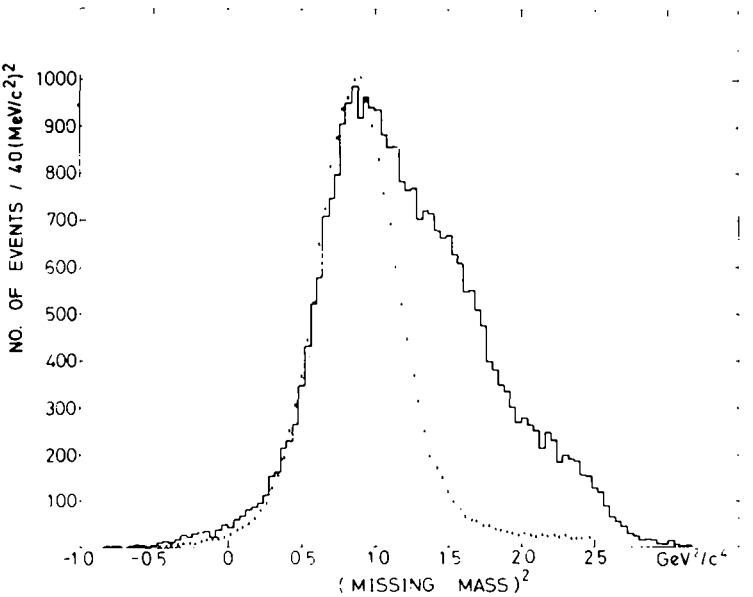

Fig. 8. Solid line: missing-mass distribution of events from "neutron loss" trigger. Crosses: missing-mass distribution of normal events.

the normal trigger plus one, and only one, of the counters $S_{5\cdot4}$, ..., $S_{5\cdot13}$, with $S_{5\cdot1}$ and $S_{5\cdot3}$ in anticoincidence. This trigger contained the neutrons that were lost in the normal trigger, and reactions of the type $\pi^- p \to \pi^+ \pi^- n (\pi^0 ...)$, where one γ-ray triggered the lead-sandwich counter. From these data we derived a correction factor, as a function of the vertex position and the neutron momentum vector. The average correction was $\langle w^{(n)} \rangle \approx 1.11$. It was determined by the following procedure:

The 30 165 neutron loss events with vertex in the target had the measured squared missing mass (MM^2) distribution shown in fig. 8. This distribution is seen to contain neutrons, and other states in the region of higher missing masses, when compared with the MM^2 distribution of normal events which is also shown in fig. 8. After eliminating from both samples the events above $MM^2 = 1.02\ \mathrm{GeV}^2/c^4$, 12, 111 neutron loss events, corresponding to 83 158 normal events recorded at the same time, were left. The known neutron direction was used to identify the counter that should have been hit, which was then compared with the one that actually gave the signal. The 10 counters $S_{5\cdot4} - S_{5\cdot13}$ surrounding the target and the 10 predicted positions gave 100 combinations which were divided into three categories: (a) signal from the one calculated to have been hit; (b) signal from a neighbour; and (c) random signal. A total of 8 007 events of category (a) were found and were then studied further; 1 611 category (b) events (which were to be expected due to neutron scatters, etc.) were included as a small correction to $\langle w^{(n)} \rangle$.

The events of category (a) have been used together with the sample of normal events to determine the mean free path d_0 for neutron interactions in scintillator leading to veto signals. Clearly, d_0 depends on the kinetic energy E_{kin} of the neutron. We verified that in all neutron energy intervals studied, the fraction of observed neutron loss events was approximately proportional to the potential path d in scintillator material. Since $d \ll d_0(E_{\mathrm{kin}})$, the neutron loss weight has been approximated by

$$w^{(n)} = 1 + \frac{d}{d_0(E_{\mathrm{kin}})} .$$

The measured veto probability per unit length of scintillator $1/d_0$ is shown in fig. 9 as a function of $\sqrt{-t} \approx \sqrt{2 m_n E_{\mathrm{kin}}}$. The whole correction is accurate to ±15% of its average value, introducing an uncertainty of ±1.7% in the rate of good events at low $|t|$, and somewhat more at $|t|$ above $0.3\ (\mathrm{GeV}/c)^2$.

3.3.4. Decaying pions

Events with secondaries that decayed along their path through the apparatus often failed reconstruction. This loss was accounted for by the weight:

$$w^{\mathrm{d}} = 1 + \left[\frac{M_\pi}{c\tau}\left(\frac{1}{p_{\pi^+}} + \frac{1}{p_{\pi^-}}\right)\right] L_{\mathrm{d}} ,$$

where L_{d} is that part of the trajectory along which a decay will produce a program

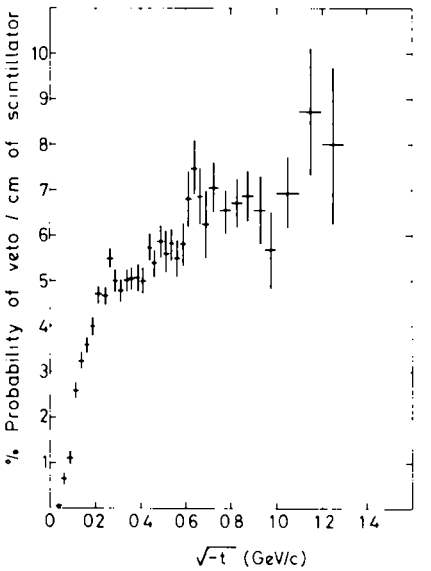

Fig. 9. % probability for a neutron to give a veto signal in 1 cm scintillator as a function of $\sqrt{-t}$.

failure, p_{π^+} and p_{π^-} are the momenta of the pions, and $c\tau$ = 780 cm. The average value of $w^{(d)}$ was 1.02.

3.3.5. Čerenkov counter inefficiencies

The efficiency of the Čerenkov counter $\check{C}_3$ to observe an event with two pions with momentum greater than 5.9 GeV/c was over 99.8% (see fig. 2). But events were lost if one pion of a pair had its momentum below the Čerenkov threshold (5 GeV/c), and the other pion interacted. From an empirical formula we calculated a global correction factor as a function of the pion momenta p_{fast}, p_{slow}:

$$w^{(c)} = 1.03 \quad 0.001 \times p_{\text{fast}}(\text{GeV}/c) , \qquad \text{if} \qquad p_{\text{slow}} < 5 \text{ GeV}/c ,$$

otherwise $w^{(c)} = 1$.

3.4. General procedure to obtain differential cross sections

The kinematics of an event can be described completely by a set of independent kinematical variables x_K which are invariant under event rotation or translation. The differential production cross section may be defined as an intensity distribution in these variables: $I_{\text{prod}}(x_K)$. At fixed beam energy we chose as kinematical variables for reaction (1) the four quantities $M_{\pi\pi}$, t, θ, ϕ, where $M_{\pi\pi}$ is the $\pi^+\pi^-$ invariant mass, t the squared four-momentum transfer between p and n, and where θ, ϕ define the π^- direction of the decaying $\pi^+\pi^-$ system, measured either in the t-channel

(Gottfried–Jackson) or s-channel helicity reference frame. To specify the configuration of an event completely, one needs in addition to x_K a set of laboratory coordinates x_L giving its position and orientation in the laboratory. Thus the distribution of event configurations in the laboratory is described by

$$I'_{\text{prod}}(x_K, x_L) = I_{\text{prod}}(x_K) P(x_L) , \tag{2}$$

where $P(x_L)$ is the spatial distribution of produced events, normalized to unity. Only part of the distribution $I'_{\text{prod}}(x_K, x_L)$ is accepted by the geometry of the detector: we call it the "accepted" distribution $I'_{\text{acc}}(x_K, x_L)$. Between I'_{prod} and I'_{acc} one has the relation

$$I'_{\text{acc}}(x_K, x_L) = A'(x_K, x_L) I'_{\text{prod}}(x_K, x_L) , \tag{3}$$

where the acceptance probability $A'(x_K, x_L)$ takes the values 1 or 0 depending on whether the event (x_K, x_L) lies inside the geometry of the apparatus or not. Integrating eq. (3) over x_L one obtains with eq. (2)

$$I_{\text{acc}}(x_K) = \int I'_{\text{acc}}(x_K, x_L) \, dx_L = A(x_K) I_{\text{prod}}(x_K) , \tag{4}$$

where the acceptance function $A(x_K)$ is defined as

$$A(x_K) = \int A'(x_K, x_L) P(x_L) \, dx_L . \tag{5}$$

Owing to the configuration-dependent detection inefficiencies discussed in subsect. 3.3, $I'_{\text{acc}}(x_K, x_L)$ is not identical to the distribution of actually observed events $I'_{\text{obs}}(x_K, x_L)$ but differs by a weight factor $w(x_K, x_L)$:

$$I'_{\text{acc}}(x_K, x_L) = w(x_K, x_L) I'_{\text{obs}}(x_K, x_L) . \tag{6}$$

In practice, $I_{\text{acc}}(x_K)$ is obtained from $I'_{\text{obs}}(x_K, x_L)$ by attaching a weight $w_i = w[x_K^{(i)}, x_L^{(i)}]$ to each individual event i, as already mentioned in subsect. 3.3.

Starting from the "accepted" distribution $I_{\text{acc}}(x_K)$, which is identical to the weighted observed distribution, relation (4) will give directly the distribution of produced events in the domain of variables x_K, where $A(x_K)$ is greater than zero.

In order to obtain $I_{\text{prod}}(x_K)$ also in the region where the acceptance is zero, one has to parametrize $I_{\text{prod}}(x_K)$ and to determine the parameters in the observed domain of variables. In subsect. 3.5 such procedures will be discussed in the context of $\pi\pi$ angular distribution fits.

The acceptance function $A(x_K)$ as defined by relation (5) has been obtained by Monte-Carlo calculation. For fixed $M_{\pi\pi}$ and t values, events were generated at random in the variables $\cos\theta$, ϕ and transformed into the lab system according to the distribution $P(x_L)$, which was derived from the measured beam distribution and the beam attenuation in the target. The acceptance $A(x_K)$ is then simply that

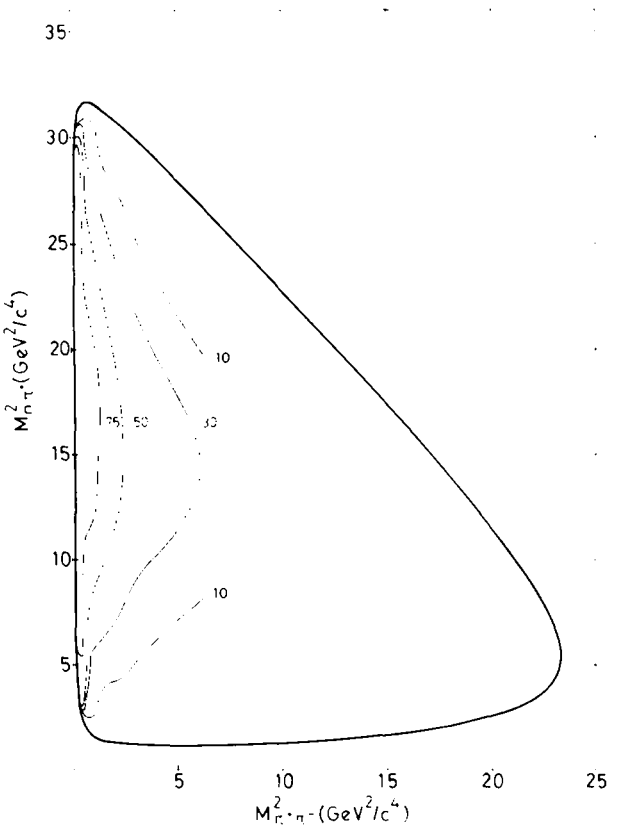

Fig. 10. Lines of equal geometric acceptance in the $\pi^+\pi^-$n Dalitz plot for events produced with constant $|t| = 0.1$ (GeV/c)^2. The acceptance is averaged over a $\pi\pi$ decay distribution isotropic in the azimuth ϕ which is defined in the s-channel helicity frame.

fraction of all events generated with x_K which lies within the accepted geometry region as defined by the magnet aperture and the arrangement of trigger counters. To avoid edge effects, the acceptance windows introduced for generated as well as for observed events were chosen somewhat smaller than the experimental ones. For each $M_{\pi\pi}$ value, Monte-Carlo calculations have been run at 18 discrete t values in the interval $0 < |t| < 1.5$ (GeV/c)^2. The spacing in $M_{\pi\pi}$ was 50 MeV/c^2. For each $M_{\pi\pi}$ and t value the average acceptance has been determined in each of 1 440 bins of size $\Delta \cos\theta \, \Delta\phi = (\frac{2}{40}) \cdot (2\pi/36)$ by generating 100 000 events for each $M_{\pi\pi}$, $|t| \leqslant 0.1$ (GeV/c)^2 and 50 000 events for each $M_{\pi\pi}$, $|t| > 0.1$ (GeV/c)^2.

Some idea of the geometrical acceptance can be obtained from fig. 10. Here lines of equal acceptance are drawn in a Dalitz diagram for the three-body final state $\pi^+\pi^-$n produced isotropically in ϕ at $|t| = 0.1$ (GeV/c)^2.

3.5. Fits to the dipion angular distribution

Owing to parity conservation in the production process (1), the most general $\pi^+\pi^-$ angular distribution with $(\cos\theta, \phi) = \Omega$ defined in the s- or t-channel helicity reference frames, or, quite generally, in any coordinate system where the y-axis is parallel to the production normal, can be written in terms of spherical harmonics $Y_L^M(\Omega)$ as follows:

$$I_{\text{prod}}(M_{\pi\pi}, t, \Omega) = \sum_{\substack{L \\ M \geqslant 0}} t_L^M \operatorname{Re} Y_L^M(\Omega) . \tag{7}$$

Here the real parameters t_L^M are functions of $M_{\pi\pi}$ and t. Since the fits to the $\pi^+\pi^-$ angular distribution were carried out in rather narrow intervals $\Delta M_{\pi\pi} \Delta t$, we consider the t_L^M as constants within one m, t bin, and omit the variables $M_{\pi\pi}$ and t from the arguments of I_{prod}. The distribution $I_{\text{prod}}(\Omega)$ was assumed to be normalized to the number of produced events N_{prod} in $\Delta M_{\pi\pi} \Delta t$:

$$\int I_{\text{prod}}(\Omega)\, d\Omega = N_{\text{prod}} = \sqrt{4\pi}\, t_0^0 . \tag{8}$$

The t_L^M are simply related to the often-used normalized spherical harmonic moments $\langle \operatorname{Re} Y_L^M \rangle$:

$$\langle \operatorname{Re} Y_L^M \rangle = \frac{1}{N_{\text{prod}}} \int I_{\text{prod}}(\Omega) \operatorname{Re} Y_L^M(\Omega)\, d\Omega = \frac{t_L^M \epsilon_L^M}{N_{\text{prod}}} , \tag{9}$$

where $\epsilon_L^M = 1$ for $M = 0$ and $\epsilon_L^M = \frac{1}{2}$ for $M \neq 0$. Throughout the rest of this paper we will simply write Y_L^M as shorthand for $\operatorname{Re} Y_L^M$. Furthermore, for simpler notation in subsequent formulae, we will also compress L, M into a single index λ, with the convention that $\lambda = 0$ corresponds to the case $L = 0, M = 0$.

Inserting eq. (7) into eq. (4) we obtain the basic relation for all angular distribution fits:

$$I_{\text{acc}}(\Omega) = A(\Omega) \sum_{\lambda=0}^{\lambda_{\max}} t_\lambda Y_\lambda(\Omega) \tag{10}$$

In the following sections, three independent fit methods are described which were employed to determine the parameters of the $\pi^+\pi^-$ angular distribution. From the χ^2 and moment method discussed below, we obtained $A(\Omega)$ for a considered $M_{\pi\pi}$, t interval by averaging the acceptance functions, calculated for fixed $M_{\pi\pi}$, t values, according to the distribution of observed events in that interval. In the maximum likelihood method $A(\Omega)$ was interpolated for each individual event.

3.5.1. χ^2 method

The procedure consists of fitting the accepted distribution I_{acc} as defined by eq. (10) to the weighted observed event distribution in a grid of $\cos\theta$, ϕ bins of equal size $\Delta\Omega$. Defining w_k as the total weight of observed events in bin k and w_k^{exp} as the expected total weight in the same bin, the χ^2 to be minimized can be written as

$$\chi^2 = \sum_k \frac{[w_k - w_k^{exp}]^2}{\sigma_k^2} , \tag{11}$$

with $w_k^{exp} = (\Delta\Omega/4\pi) A(\Omega_k) \Sigma_\lambda t_\lambda Y_\lambda(\Omega_k)$.

In the fits $Y_\lambda(\Omega_k)$ was evaluated at the bin centre whereas for $A(\Omega_k)$ the average acceptance in the bin was used. The squared variance of the expected total weight w_k^{exp} can be shown to be

$$\sigma_k^2 = \frac{\langle w_k^2 \rangle}{\langle w_k \rangle} w_k^{exp} , \tag{12}$$

where $\langle w_k \rangle$ is the mean event weight in bin k and $\langle w_k^2 \rangle$ the mean squared weight. Since our weights depend only very weakly on $\cos\theta$, ϕ, constant values $\langle w \rangle$ and $\langle w^2 \rangle$, evaluated from all events included in the fit, have been used for all bins. The same bin size $\Delta\Omega = (2/40) \cdot (2\pi/36)$ has been chosen as in the acceptance calculation. Owing to parity conservation, the angular distribution to be fitted has the property $I_{prod}(\theta, \phi) = I_{prod}(\theta, 2\pi - \phi)$. Therefore the fits were performed in only half the $\cos\theta, \phi$ plane by summing observed events and averaging acceptance over corresponding bins $(\cos\theta_k, \phi_k)$ and $(\cos\theta_k, 2\pi - \phi_k)$. Bins with $A(\Omega_k) < 0.02$ have been excluded from the fit.

The χ^2 minimization was achieved by solving the system of equations $\partial\chi^2/\partial t_\lambda = 0$ for t_λ with standard iterative procedures. Three to four iteration steps were necessary to reach convergence. The error matrix $E(t_\mu)$ of the fitted t_λ was obtained from the relation

$$[E(t_\mu)^{-1}]_{\lambda\lambda'} = \frac{1}{2} \frac{\partial^2 \chi^2}{\partial t_\lambda \partial t_{\lambda'}} . \tag{13}$$

3.5.2. Linear algebra method (method of moments)

Multiplying eq. (10) with $Y_{\lambda'}(\Omega)$ and integrating over Ω yields

$$\int I_{acc}(\Omega) Y_{\lambda'}(\Omega) \, d\Omega = \sum_\lambda \{ \int Y_{\lambda'}(\Omega) A(\Omega) Y_\lambda(\Omega) \, d\Omega \} t_\lambda . \tag{14}$$

For easier notation we define the experimental moments

$$b_\lambda = \int I_{acc} Y_\lambda \, d\Omega \ , \tag{15}$$

and the acceptance correlations

$$A_{\lambda'\lambda} = \int Y_{\lambda'} A \, Y_\lambda \, d\Omega \ . \tag{16}$$

Thus eq. (14) can be rewritten in simpler form:

$$b_{\lambda'} = \sum_\lambda A_{\lambda'\lambda} t_\lambda \ . \tag{17}$$

For a set of different λ', relation (17) defines a system of linear equations which can be solved for the t_λ as soon as one employs as many equations as there are t_λ admitted. Using more equations than unkowns yields an over-determination allowing for a real fit which will reduce the errors in t_λ. This fit is achieved by minimizing

$$\chi^2 = \sum_{\mu\mu'} d_\mu [E(b)^{-1}]_{\mu\mu'} d_{\mu'} \ , \tag{18}$$

where

$$d_\mu = \sum_\lambda A_{\mu\lambda} t_\lambda \quad b_\mu \ ,$$

and where $E(b)$ is the error matrix of the experimental moments b_μ. In eq. (18) we have neglected possible errors in the acceptance correlations $A_{\mu\lambda}$ which in principle can be calculated to any required precision. The minimization of the χ^2 defined in eq. (18) is still a linear problem which is solved by standard methods of matrix algebra.

In practice the b_λ, as defined by eq. (15), are obtained by summing over observed events:

$$b_\lambda = \sum_{i=1}^{N_{obs}} w_i \, Y_\lambda(\Omega_i) \ , \tag{19}$$

where w_i is the weight of event i and N_{obs} the number of observed events included in the fit. Similarly the acceptance correlations are calculated by summation over acceptance bins in the Monte-Carlo calculation:

$$A_{\lambda'\lambda} = \frac{4\pi}{N_{gen}} \sum_{j=1}^{N_{bins}} n_i \, Y_{\lambda'}(\Omega_i) \, Y_\lambda(\Omega_i) \ , \tag{20}$$

where n_i is the number of accepted events in each of the 1440 $\cos\theta, \phi$ bins, N_{gen}

the number of generated events in the Monte-Carlo calculation, and $Y_\lambda(\Omega_i)$ the values of the spherical harmonics in the centre of the bin. The error matrix of the experimental moments b_λ is

$$E(b)_{\mu\mu'} = \sum_{i=1}^{N_{obs}} w_i^2 Y_\mu(\Omega_i) Y_{\mu'}(\Omega_i) . \tag{21}$$

From $E(b)$ and the acceptance correlation matrix A, one obtains the error matrix $E(t)$ of the fitted expansion coefficients t_λ. In matrix notation we have

$$E(t) = [A^T E(b)^{-1} A]^{-1} . \tag{22}$$

The fitted t_λ presented in sect. 4 have been obtained from an overdetermined system of 45 equations corresponding to all indices λ' from $L' = 0, M' = 0$ to $L' = 8, M' = 8$.

3.5.3. Maximum likelihood method

The maximum likelihood method was applied to the distribution of accepted events

$$I_{acc}(\Omega) = A(\Omega) \sum_\lambda t_\lambda Y_\lambda(\Omega), \tag{23}$$

which was normalized to the total weight w of all events participating in the fit:

$$\int I_{acc}(\Omega)\, d\Omega = w . \tag{24}$$

Inserting a spherical harmonic expansion of the acceptance

$$A(\Omega) = \sum_\lambda a_\lambda Y_\lambda(\Omega) \tag{25}$$

into eq. (24) one obtains the normalization constraint as a linear relation between the t_λ:

$$t_0 = \frac{1}{a_0} \left[w - \sum_{\lambda > 0} t_\lambda a_\lambda \epsilon_\lambda \right] . \tag{26}$$

When using the orthonormality of spherical harmonics to obtain eq. (26) the factor $\epsilon_\lambda = \epsilon_L^M$ occurs, already defined in subsect. 3.5, since Y_λ stands for Re Y_L^M. With eq. (26) we can rewrite I_{acc} in an already properly normalized form:

$$I_{acc}^N(\Omega) = A(\Omega) I_{prod}^N(\Omega) ,$$

where

$$I^N_{\text{prod}}(\Omega) = \frac{Y_0}{a_0} w + \sum_{\lambda \neq 0} \left[Y_\lambda(\Omega) - \frac{Y_0}{a_0} a_\lambda \epsilon_\lambda \right] t_\lambda . \tag{27}$$

Omitting constant factors, the ith event in the set with its weight w_i will then contribute to the likelihood function $\mathcal{L}$ the factor

$$p_i = [I^N_{\text{prod}}(\Omega_i)]^{w_i} . \tag{28}$$

The expansion coefficients a_λ were obtained as moments of the accepted Monte-Carlo events. Each observed event i obtained individual coefficients a^i_λ which resulted from an interpolation in the Monte-Carlo $M_{\pi\pi}$, t grid. The logarithmic likelihood function

$$\log \mathcal{L} = \sum_i \log p_i \tag{29}$$

was maximized by the CERN routine MINUIT thus yielding the most probable set of coefficients t_λ. MINUIT also evaluated the errors of t_λ requiring a change of $\frac{1}{2}$ in $\log \mathcal{L}$ when moving off the maximum. The errors obtained in this way had to be corrected for the introduction of individual weights. They were multiplied by the square root of the average weight $\sqrt{\langle w \rangle}$. The method described is strictly correct when applied to small $M_{\pi\pi}$ and t.

3.5.4. Comparison of the three methods

A detailed comparison of the three fitting procedures has been performed in several $\Delta M_{\pi\pi} \Delta t$ bins with large event statistics ($> 3\,000$). Perfect agreement was found between the angular distribution moments obtained by the different methods. the deviations between individual results being considerably smaller than the statistical errors. Also the errors in the fitted quantities revealed full equivalence of the applied methods. Once this equivalence had been established, only the χ^2 and the moment methods were applied since they consumed far less computer time than the maximum likelihood procedure.

3.5.5. Consistency checks for the determination of the spherical harmonic moments

We performed several tests to investigate the consistency and reliability of the moments extracted from the data:

3.3.5.1. Measurement of the imaginary parts of the spherical harmonic moments

Imaginary parts of the moments, although forbidden by parity conservation, could be observed in the unweighted data owing to asymmetries of our apparatus. However, after all acceptance corrections, we expect them to vanish. In fig. 11 we

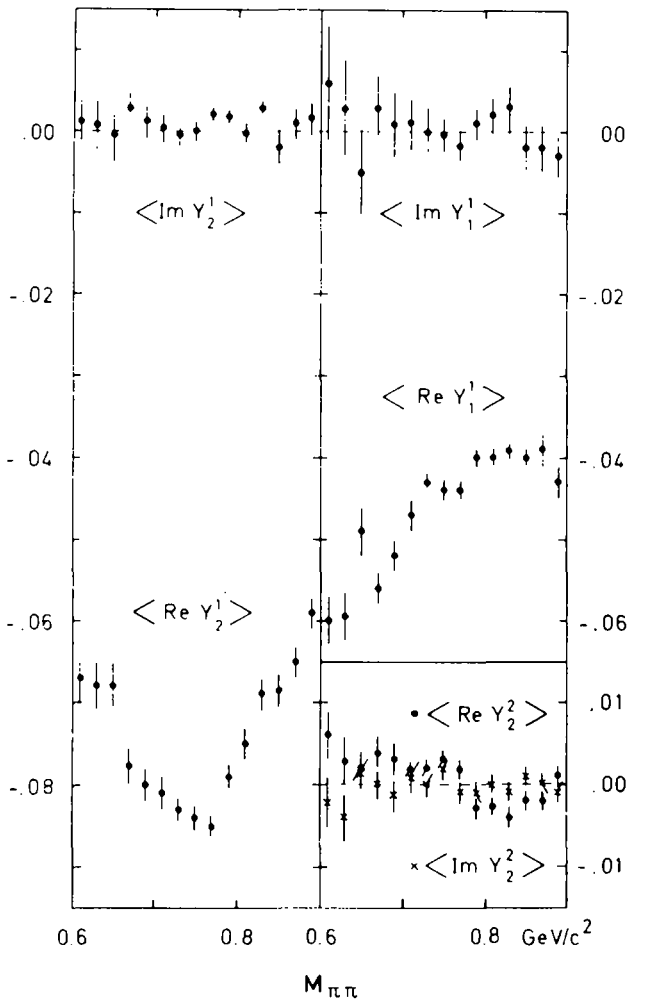

Fig. 11. Real and imaginary parts of $\langle Y_L^M \rangle$ *versus* $M_{\pi\pi}$ for $L \leq 2, M \leq 2$ and $|t| < 0.15$ GeV$^2/c^2$.

show the real and imaginary parts of Y_L^M for $L \leq 2$ and $M \leq 2$, in the dipion mass region from 0.660 to 0.850 GeV/c^2. The imaginary parts are everywhere consistent with zero within statistics; furthermore, no small systematic deviations from zero or correlations with the real parts of the moments can be observed.

3.5.5.2. Comparison of distributions observed in the lab. with Monte-Carlo generated distributions

We used the values of t_λ determined in this experiment as input to a Monte-Carlo program generating events in the laboratory system. We constructed the accepted

event distribution $I'_{acc}(x_K, x_L)$ as given by eq. (3), in the mass region $0.62\ \mathrm{GeV}/c^2 < M_{\pi\pi} < 0.92\ \mathrm{GeV}/c^2$ and for values of momentum transfer $-0.75\ (\mathrm{GeV}/c)^2 < t < -0.02\ (\mathrm{GeV}/c)^2$ with $d\sigma/dt = \mathrm{const} \cdot \exp(14.2\,t)$. We could not find any significant deviation of the observed distribution from the Monte-Carlo generated distribution.

3.6. N^* reflections

When investigating $\pi\pi$ angular distributions it appears meaningful to cut out final states where the two π's evidently do not arise from a common (temporarily bound) system of relatively low angular momentum. Clearly final states $N^*\pi$ when $N^* \to n\pi$ is a narrow resonance such as the $\Delta(1236)$, should be excluded from the $\pi\pi$ angular analysis.

The way to proceed is less clear when one deals with a broad N^* enhancement such as the diffractively produced $I = \frac{1}{2}$ $N\pi$ system in the mass range between 1.1 and 1.8 GeV/c^2 [19, 20]. The data of ref. [19] suggest that the width of the diffractive N^* enhancement does not increase with beam energy. Assuming this to be established, it is evident that the influence of the N^* on the $\pi\pi$ angular distribution at fixed $\pi\pi$ mass becomes less and less important with increasing energy. Therefore we consider it as the more correct procedure to cut out the N^* even at intermediate energies where it still has non-negligible effects on the $\pi\pi$ angular distribution. There exist other viewpoints on this particular question [21].

Our apparatus does not accept any $n\pi^+$ and $n\pi^-$ invariant masses below 1.5 GeV/c^2. Therefore the fitted $\pi^+\pi^-$ angular distributions are free from distortions caused by the $\Delta(1236)$ final state. However, higher lying N^* resonances diffractively produced might have some influence on the fitted moments.

To investigate this question we have recalculated, with the appropriate acceptance functions, the moments of our observed distributions after first excluding all events with a nucleon-π mass less than 2 GeV/c^2. This removed, 9%, 15% and 12% of the events in the ρ, f and g regions, respectively.

For $|t| < 0.15\ (\mathrm{GeV}/c)^2$ the recalculated moments were distributed randomly around the moments of figs. 14 and 15 within the expected statistical fluctuations for all Y_L^M and $M_{\pi\pi}$ except for one set of deviations. These were a systematic decrease of $Y_L{}^0$ and an increase of Y_L^1 ($L = 1, 2, \ldots, 6$) by about one standard deviation of a single measurement point (~ 0.015) in the mass range 900–1500 MeV/c^2. We have no interpretation for this small but statistically significant effect.

For $|t| > 0.5\ (\mathrm{GeV}/c)^2$ there appear to be deviations of a few standard deviations in some (small) moments. No systematic trends could be discerned.

3.7. Absolute cross section

The fitted distribution of produced events $I_{prod}(x_K)$ as defined in subsect. 3.4 is corrected only for configuration-dependent losses. In order to obtain an absolute

cross section one has to consider in addition a number of losses which are independent of the event kinematics and geometry and can therefore be accounted for by applying a constant global weight factor w_g to $I_{\text{prod}}(x_K)$. In the following we list all the configuration-independent corrections contributing to this common weight factor, which was found to be $w_g = 1.53 \pm 0.05$.

(1) Reconstruction losses:
losses due to extra beam tracks in the spark chambers during their sensitivity time $= 9.4 \pm 0.2\%$,
for partial chamber inefficiency $= 2.0 \pm 1.0\%$,
for wrong spark pairing or sorting $= 2.5 \pm 1.0\%$.

(2) Losses due to electronics inefficiency:
inefficiency of the interaction sensing counter S_7 $= 0.8 \pm 0.4\%$,
losses of triggers due to dead time of the selection system associated with the anticoincidence counters $= 5.9 \pm 0.5\%$.
inefficiencies associated with counter array S_9 $= 1.2 \pm 0.5\%$,
losses due to a third array counter counting $= 2.5 \pm 0.3\%$,
second beam particle arriving within 0.5 μsec after event $= 2.5 \pm 0.1\%$,
accidental count causing two triggering reactions to be "flagged" $= 1.2 \pm 0.6\%$.

(3) Loss of secondary π^+ and π^- due to interaction in the apparatus $= 5.2 \pm 0.1\%$,

(4) Selection of missing neutron by applying a χ^2 cut loss $= 4.5\%$,

(5) Beam contamination: $2.5 \pm 2.0\%$ muons; $0.4 \pm 0.2\%$ electrons.

(6) Contribution of $\pi^+\pi^-(\pi^0 n)$ final state $= -2.6 \pm 0.9\%$.

(7) Beam attenuation in target $= 2.4\%$.

(8) Loss of events due to the dead space in the counter array $= 1.7 \pm 0.1\%$.

(9) Correction for the target walls $= -0.9 \pm 0.1\%$.

(10) Contribution of K^+K^- or $p\bar{p}$ final state to the $\pi^+\pi^-$ spectrum $= -0.7 \pm 0.1\%$.

(11) Interaction loss of beam in front of the target $= 0.5 \pm 0.1\%$.

The absolute calibration of the cross section was obtained from a sample of 42 000 good events, which had been taken under particularly stable running conditions. Normalizing the result to the total number of events included in the present analysis, we find that one produced event corresponds to a cross section of

$$0.106 \pm 0.005 \text{ nb}. \tag{30}$$

From this value and the fitted distribution of observed events one determines the production cross section for reaction (1) in the interval of $0.6 < M_{\pi\pi} < 0.94$ GeV/c^2, $|t| < 0.15$ (GeV/c)^2 to be

$$\sigma(\pi^- p \to \pi^-\pi^+ n) = (35.0 \pm 1.7)\,\mu\text{b}.$$

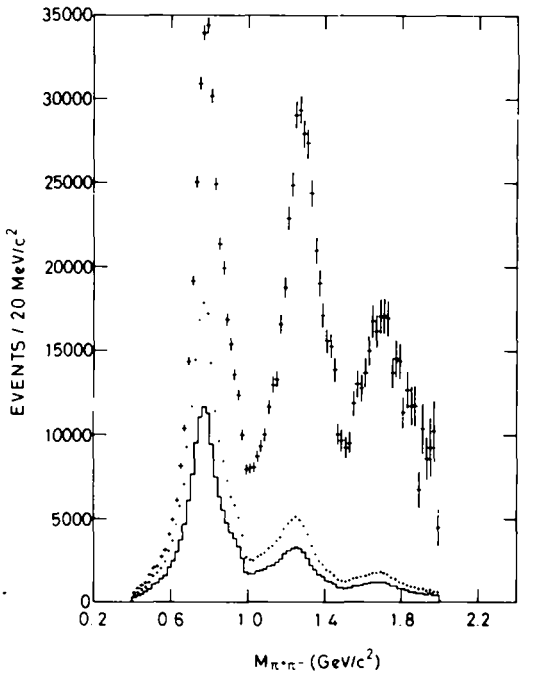

Fig. 12. $\pi^+\pi^-$ invariant mass spectrum for events with $|t| < 0.15\ \mathrm{GeV}^2/c^2$, in 20 MeV/$c^2$ $M_{\pi\pi}$ bins. Histogram: observed events. Dots: weighted observed events. Points with error bars: produced events.

4. Experimental results

4.1. $\pi^+\pi^-$ mass spectrum

Using the methods described in sect. 3 we have determined the corrected number of events and their angular distribution in various $M_{\pi\pi}$, t intervals. Fig. 12 shows the $\pi^+\pi^-$ mass spectrum in bins of 20 MeV/c^2 up to $M_{\pi\pi} = 2$ GeV/c^2 for $-t < 0.15$ (GeV/c)^2. The solid line histogram represents the spectrum of observed events; the points correspond to the number of "accepted" or weighted observed events, see eq. (6); and finally the points with error bars give the number of produced events obtained from angular distribution fits in the Gottfried–Jackson frame, with $L_{\max} = 6$, $M_{\max} = 2$. The angular distribution in the $M_{\pi\pi}$ and t range considered here was found not to contain any significant moments with $L > 6$ or $M > 2$, except perhaps for the Y_7^0 and Y_7^1 moments which show, as discussed in subsect. 4.2, slight deviations from zero in the g-meson mass region. From fig. 12 it follows that production of the ρ, f and g resonances are clearly the dominant con-

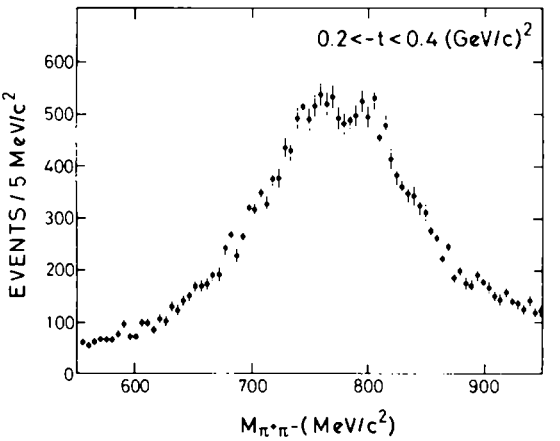

Fig. 13. $\pi^+\pi^-$ invariant mass spectrum in the interval $0.2 < -t < 0.4\ \mathrm{GeV}^2/c^2$.

tributions to the cross section in the considered range of variables. The error bars on the cross section increase with $\pi\pi$ mass owing to decreasing geometric acceptance and an increasing number of angular momentum states produced.

In fig. 12, and all subsequent figures, one produced event (i.e. one event in a distribution corrected for acceptance) corresponds to a cross section of $(1.06 \pm 0.05) \times 10^{-34}\ \mathrm{cm}^2$.

The ρ and f mesons are observed with shoulders on their high mass sides. Whereas the shoulder around 980 MeV/c^2 just reflects the energy dependence of the $\pi\pi$ S-wave intensity (see subsect. 4.2), we have no explanation for the shoulder in the f region at around 1460 MeV/c^2 which is observed in both the moments $N\langle Y_2^0 \rangle$ and $N\langle Y_4^0 \rangle$.

We have examined our data for possible narrow structures in the mass spectrum. Finer mass binning than that of fig. 12 for low as well as for high values of t could not establish any of the following effects which have been observed in $\pi^+\pi^-$ mass spectra, or other particle systems with the same allowed quantum numbers:

(i) the claimed four standard deviation peak centered at 665 MeV/c^2 in $\pi^+\pi^-$ effective mass [22];

(ii) narrow enhancements [15, 23, 24] in the mass range 940–1020 MeV/c^2;

(iii) $\eta_N(1080)$ as described in the tables of the Particle Data Group [23, 24];

(iv) split f meson [23, 24].

The only narrow structure that can be seen in the mass spectrum is that arising from $\rho - \omega$ interference at large $-t$ values. A detailed analysis of these data will soon be published [25]. Fig. 13 shows the effect in our data for $0.2 < |t| < 0.4\ (\mathrm{GeV}/c)^2$.

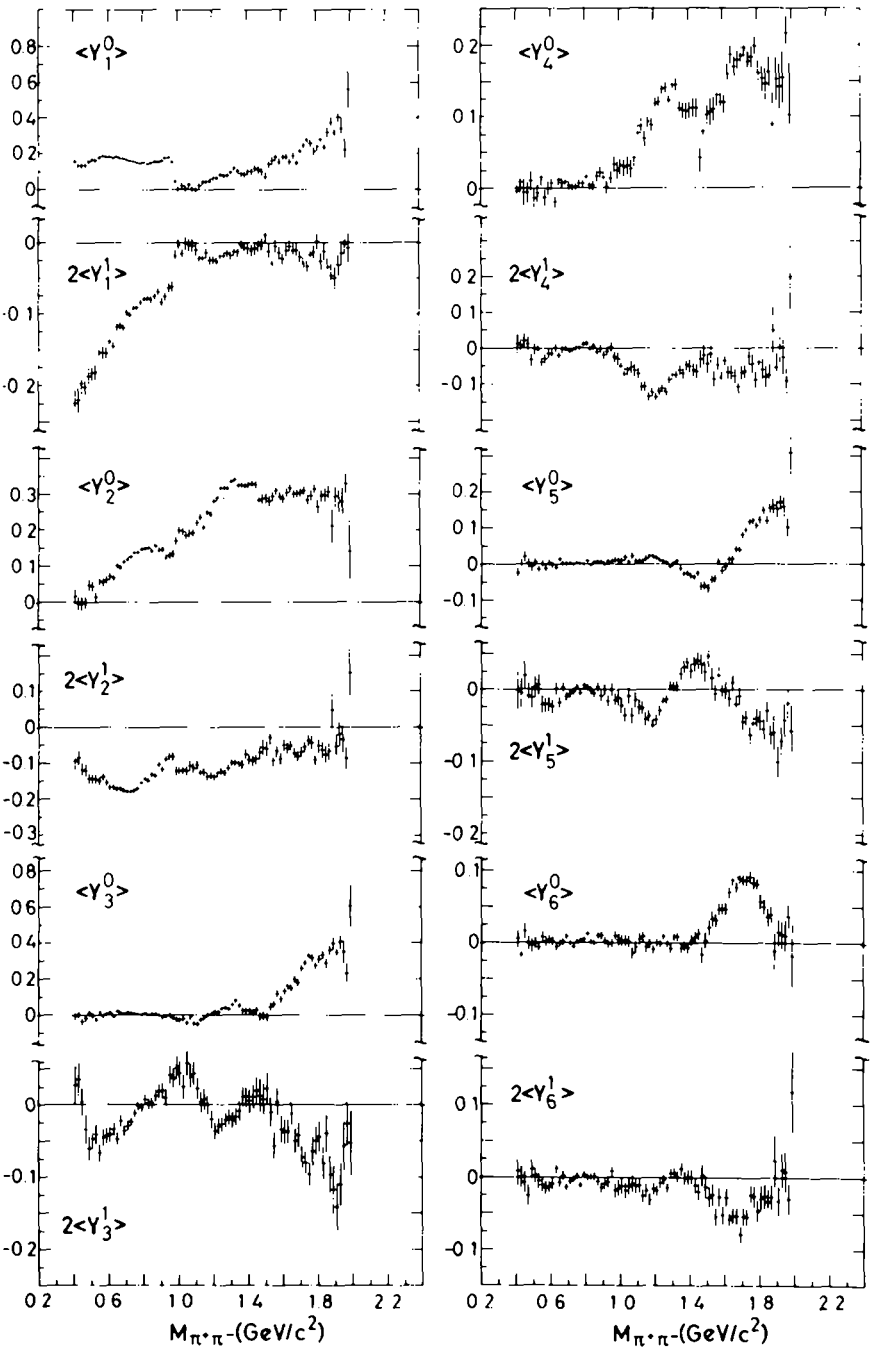

Fig. 14. Mass dependence of $\pi^+\pi^-$ angular distribution moments $\langle Y_L^0 \rangle$ and $\langle Y_L^1 \rangle$ for Gottfried–Jackson frame. The values are averaged over the interval $|t| < 0.15$ GeV^2/c^2 and were obtained from fits determining all $\langle Y_L^M \rangle$ up to $L_{max} = 6$, $M_{max} = 2$.

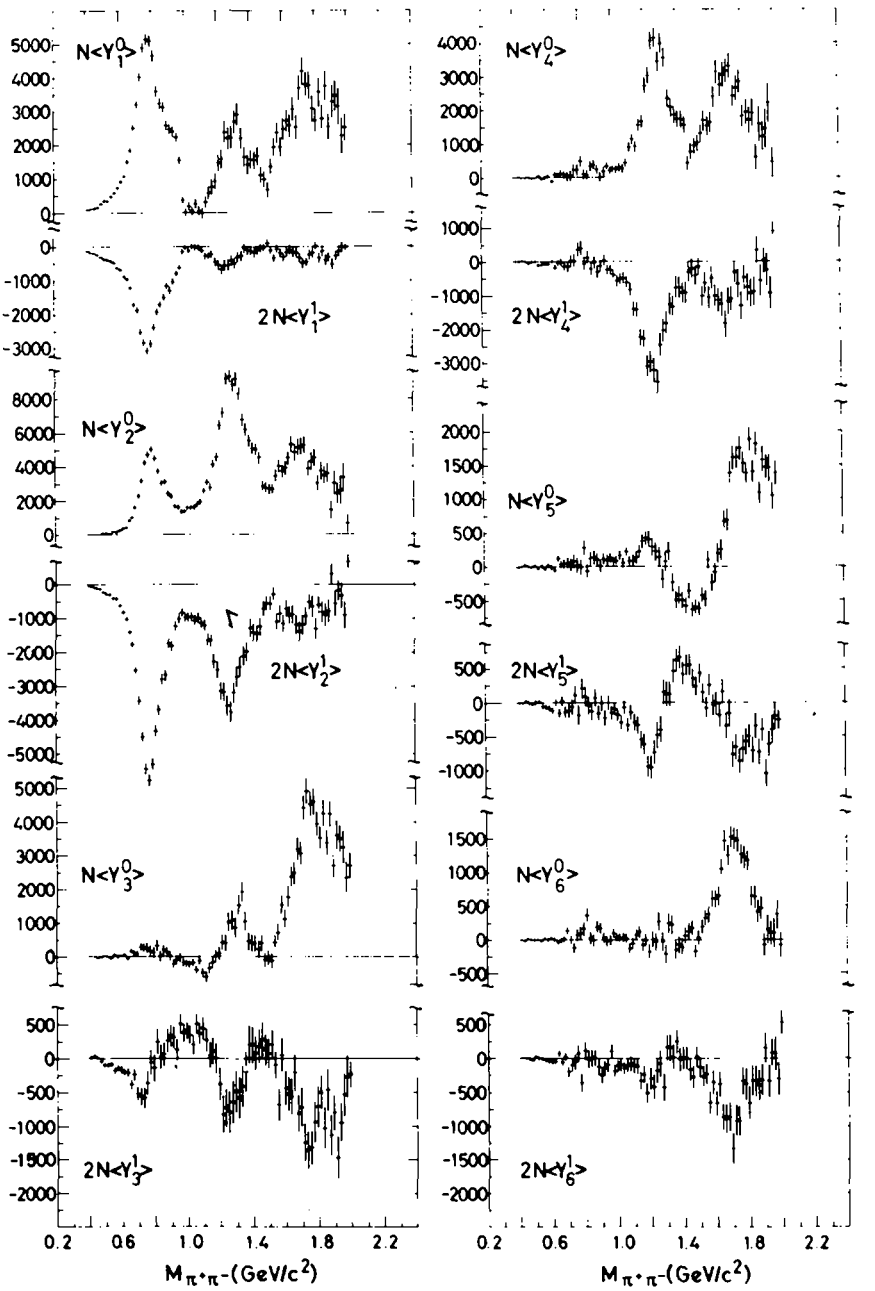

Fig. 15. Mass dependence of $N_{\text{prod}}\langle Y_L^0\rangle$ and $N_{\text{prod}}\langle Y_L^1\rangle$ corresponding to specifications of fig. 14.

4.2. Mass dependence of the $\pi^+\pi^-$ angular distribution

In fig. 14 we show for the Gottfried–Jackson frame the normalized spherical harmonic moments $\langle Y_L^0 \rangle$ and $\langle Y_L^1 \rangle$ of the $\pi^+\pi^-$ angular distribution for $-t < 0.15$ $(\mathrm{GeV}/c)^2$. The corresponding unnormalized moments $N\langle Y_L^0 \rangle$, $N\langle Y_L^1 \rangle$, where N is the number of produced events per $M_{\pi\pi}$, t bin, are plotted in fig. 15. The moments in figs. 14 and 15 were obtained from the same fits as the corrected mass spectrum of fig. 12. Moments with $M > 2$ are found to be negligible in the range $-t < 0.15$ $(\mathrm{GeV}/c)^2$. Above 600 MeV/c^2 even the Y_L^2 moments are compatible with zero.

Below 600 MeV/c^2, $\langle Y_2^2 \rangle$ and $\langle Y_3^2 \rangle$ rise to a small but statistically significant value of around 0.03. While we cannot explain how this happens, it is possible that it may be due to a systematic bias in measurement or reconstruction of very small opening angle events.

Reaction (1) is known [17] to be dominated by one-pion exchange in the t range considered in figs. 14 and 15. For one-pion exchange without absorption the angular distribution should contain only Y_L^0 moments in the Gottfried–Jackson frame. Thus the qualitative features of $\pi^+\pi^-$ scattering can be discussed by considering the mass dependence of $\langle Y_L^0 \rangle$ or $N\langle Y_L^0 \rangle$ only.

First we recall that the highest moment $\langle Y_L \rangle$ generated by a certain angular momentum state l is $\langle Y_{2l} \rangle$, and that therefore the highest even L moment $\langle Y_{2l} \rangle$ will usually project out some pure spin l part from the total $\pi\pi$ intensity. For instance, in the ρ region $N\langle Y_2^0 \rangle$ will give a better description of the shape of the ρ resonance than the mass spectrum which contains a substantial amount of $\pi\pi$ S-wave. As can be seen from figs. 14 and 15, the shoulder in the mass spectrum at 0.98 GeV/c^2 which is caused by a rapidly changing S-wave intensity is observed in the S-P interference term $N\langle Y_1^0 \rangle$ but not in $N\langle Y_2^0 \rangle$. Similar arguments hold for the terms $N\langle Y_4^0 \rangle$ or $N\langle Y_6^0 \rangle$ with respect to the shape of the f or g resonances, respectively. Of course the observed mass dependence of $N\langle Y_6^0 \rangle$ simultaneously establishes the spin of the g meson to be three, as already shown in a previous paper [3]*. We shall use these spin projection properties of the $L = 2$, $L = 4$, and $L = 6$ moments in subsect. 4.6 to determine the resonance parameters of the ρ, f and g mesons respectively.

From the moments with odd L, one can learn about the interference between odd and even angular momentum states. For this purpose it is sometimes more instructive to look at the normalized moments $\langle Y_L^M \rangle$ rather than at $N\langle Y_L^M \rangle$. The quantity $\langle Y_1^0 \rangle$ shows the well-known relatively constant behaviour in the ρ region up to a mass of 0.98 GeV/c^2. Then it drops abruptly to zero within an interval of ~ 15 MeV/c^2. This sudden change of $\langle Y_1^0 \rangle$ at a $\pi^+\pi^-$ mass of 0.98 GeV/c^2, together with the intensity drop at about the same mass, has been attributed [2,26,27]

* An inefficiency in our reconstruction program had led to negative Y_6^0 moments for certain mass intervals below the g meson, as shown in early moment plots of ref. [3]. This error is now eliminated.

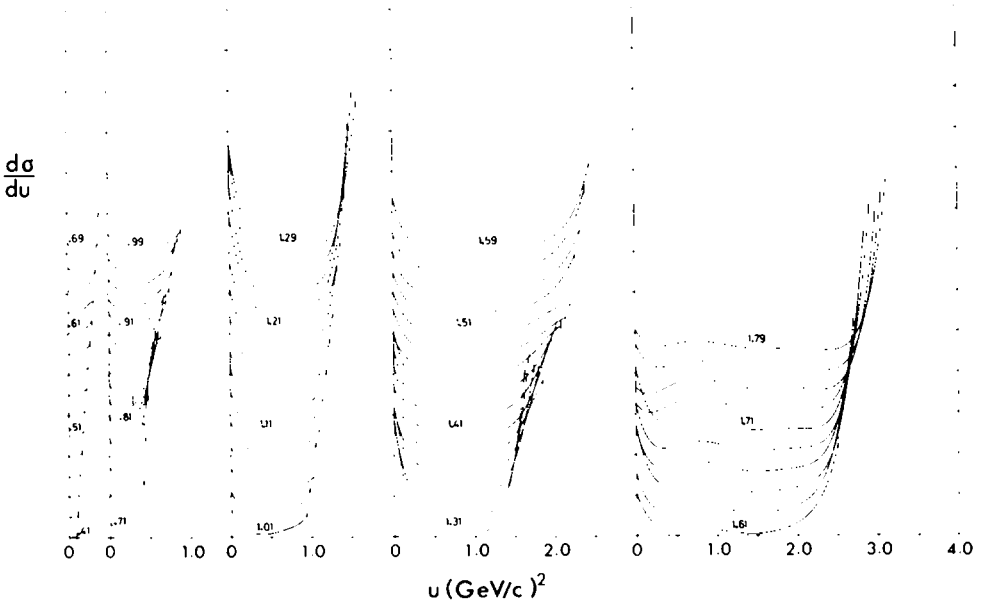

Fig. 16. $d\sigma/du$ ($\pi^+\pi^- \to \pi^+\pi^-$) as a function of u. Each curve represents a $\pi^+\pi^-$ mass bin of 20 MeV/c^2 (the central value is written on the curve) and is displaced by $\frac{1}{2}$ scale unit. 1 scale unit $\hat{=}$ 20 000 events.

to the opening of the inelastic $K\bar{K}$ channel in $\pi^+\pi^-$ scattering. Furthermore, as the phase-shift analyses of our experiment [4,10,12] and the analysis of Protopescu et al. [28] have shown, the data indicate an extremely fast rising $I = 0$ S-wave phase shift δ_S^0 in the mass region between 0.92 GeV/c^2 and KK threshold. Protopopescu et al. [28] have attributed the observed phenomenon to the joint effect of the opening of the $K\bar{K}$ channel and the presence of an S^* pole very close to the $K\bar{K}$ threshold. Between 1 and 2 GeV/c^2, $\langle Y_1^0 \rangle$ rises almost linearly with the $\pi^+\pi^-$ mass.

An alternative explanation of the rapid drop of $\langle Y_1^0 \rangle$ has been given by Odorico [29] in terms of a systematic appearance of amplitude zeros in $\pi\pi$ scattering. These should give minima in the $\pi^+\pi^- \to \pi^+\pi^-$ angular distribution at constant

$$u = [p(\pi_{in}) - p(\pi^+_{out})]^2 . \tag{31}$$

Fig. 16 shows [4] the angular distribution $d\sigma/du$ for different intervals of $\pi\pi$ mass obtained from the moments of fig. 15. The minima indeed stay at approximately constant u.

The Y_3^0 moment becomes significantly non-zero above $M_{\pi\pi} = 0.6$ GeV/c^2, thus establishing clearly the presence of a D-wave in the ρ region. After a smooth increase with mass, $N\langle Y_3^0 \rangle$ changes its slope and crosses zero at ~ 0.8 GeV/c^2, indicating

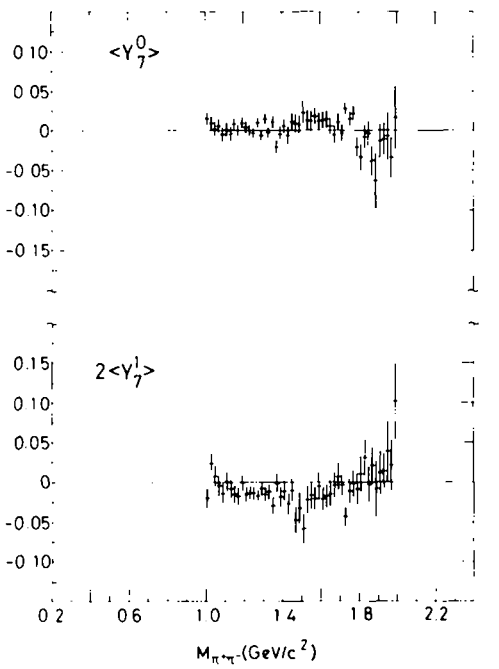

Fig. 17. $\langle Y_7^0 \rangle$, $\langle Y_7^1 \rangle$ obtained from fits with $L_{max} = 7$, $M_{max} = 1$. Other specifications as for fig. 14.

that at this mass the complex P- and D-wave amplitudes in the Argand diagram become perpendicular to each other. (The corresponding behaviour of $N\langle Y_3^1 \rangle$ is even more pronounced, though with opposite sign.) Between 0.8 and 1.2 GeV/c^2, $N\langle Y_3^0 \rangle$ stays negative, showing that the phase angle between the P- and D-wave is $> 90°$ in this region. Above a mass of 1.1 GeV/c^2 the resonant D-wave amplitude changes rapidly with energy. At 1.2 GeV/c^2, just below the f-meson resonant mass, it becomes again perpendicular to the now relatively stationary P-wave amplitude, thus causing $N\langle Y_3^0 \rangle$ to cross zero with positive slope. Positive $N\langle Y_3^0 \rangle$ above 1.2 GeV/c^2 also indicates that the real part of the P-wave is still negative in this mass region. Above 1.3 GeV/c^2 the contribution of D-F interference to the Y_3^0 moment becomes important and causes a change in the $N\langle Y_3^0 \rangle$ slope. $N\langle Y_3^0 \rangle$ reaches a minimum at 1.5 GeV/c^2, as does the Y_5^0 moment, since D-F interference is now the dominant contribution to $N\langle Y_3^0 \rangle$. With further increasing mass, $N\langle Y_5^0 \rangle$ and $N\langle Y_3^0 \rangle$ show a very similar behaviour.

The moment $N\langle Y_5^0 \rangle$, representative of D-F interference, is already present at a mass of 1 GeV/c^2. Its mass dependence in the f and g regions can be discussed in complete analogy to that of $N\langle Y_3^0 \rangle$ in the ρ and f regions.

In a special angular distribution fit the moments $\langle Y_7^0 \rangle$ and $\langle Y_7^1 \rangle$ were not constrained to zero but included as free parameters. They are displayed in fig. 17.

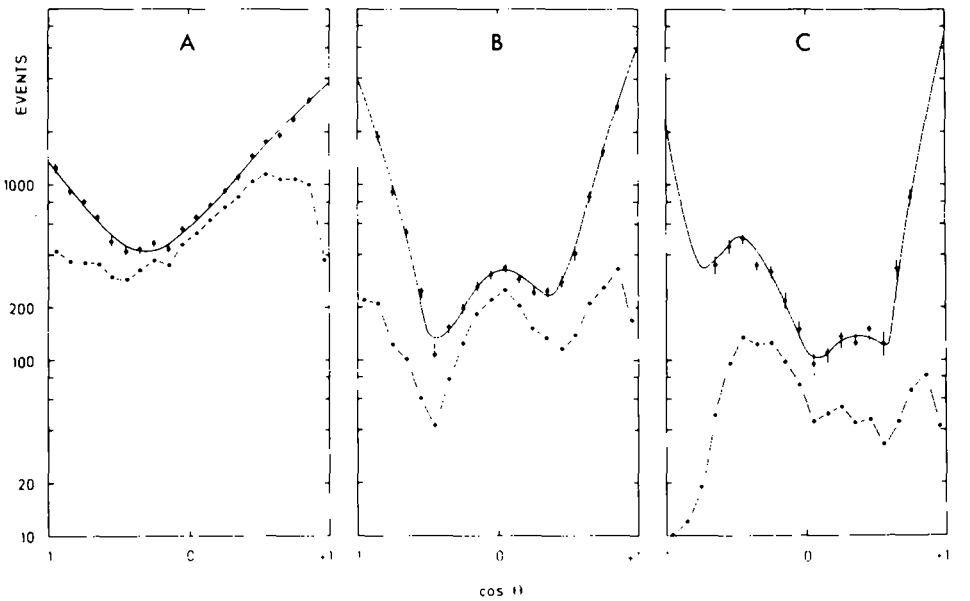

Fig. 18. Event distribution in $\cos\theta$ after integration over ϕ, for $|t| \leq 0.15$ (GeV/c)^2 for intervals of $M_{\pi\pi}$: (A) $760 \leq M_{\pi\pi} \leq 780$ MeV/c^2, (B) $1260 \leq M_{\pi\pi} \leq 1280$ MeV/c^2, (C) $1700 \leq M_{\pi\pi} \leq 1720$ MeV/c^2. Dots: measured distribution. Points with error bars: produced distribution. Continuous curve: results of fit.

Although $\langle Y_7^0 \rangle$ and $\langle Y_7^1 \rangle$ are compatible with zero over most of the mass range, there is an indication that these moments cross zero in the g region in a way expected for a resonant $l = 3$ wave interfering with an almost real $l = 4$ amplitude.

In fig. 18 we show the distribution in $\cos\theta$ after integration over ϕ, for $|t| < 0.15$ (GeV/c)^2, for intervals of $M_{\pi\pi}$ in the ρ-, f- and g-meson regions. The bare points show the number of events recorded, the points with error bars the number of events produced, calculated for those $\cos\theta$ values for which the acceptance was greater than 0.02 for all ϕ. The continuous line gives the distribution fitted by the method of subsect. 3.5.1. As in all elastic scattering processes, the forward peak increases with increasing $\pi\pi$ energy.

The moments $\langle Y_L^1 \rangle$ which are forbidden in the OPE model show a striking similarity to the $\langle Y_L^0 \rangle$ moments in their mass dependence except for their opposite sign (figs. 14 and 15). This similarity can best be visualized by plotting the ratios $\langle Y_L^0 \rangle / \langle Y_L^1 \rangle$ which are shown in fig. 19 for regions where $|\langle Y_L^1 \rangle|$ is not too small. These ratios (especially for even L) do not show the strong resonant behaviour of the original moments, but they all show the same trend of decreasing with increasing $\pi\pi$ mass. These properties of the ratios suggest that the helicity amplitudes for the production of $\pi\pi$ states with angular momentum l factorize into the $\pi\pi$ partial-wave amplitudes T_l and a weakly mass-dependent part, as suggested by Schlein [30,31].

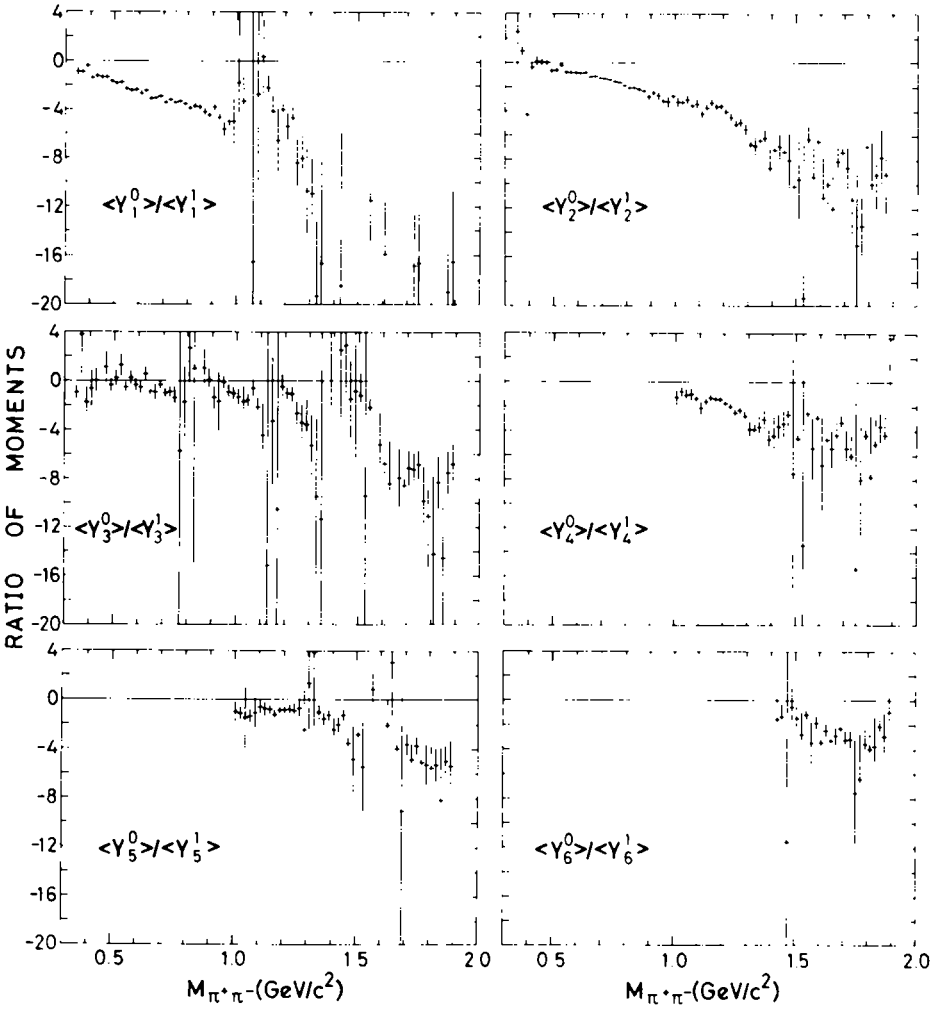

Fig. 19. Mass dependence of ratios $\langle Y_L^0 \rangle / \langle Y_L^1 \rangle$. The $\langle Y_L^M \rangle$ were determined in Gottfried–Jackson frame for $|t| < 0.15$ GeV$^2/c^2$.

The factorization property alone, however, does not account for the fact that these ratios have a rather smooth mass dependence over the entire mass interval considered in fig. 19, whereas the relative contributions of the various partial waves to one particular moment change. It has been shown recently by Ochs and Wagner [32] that this effect can be understood in terms of the "poor man's absorption model" [33] (see below) which predicts both the $\langle Y_L^0 \rangle$ and the $\langle Y_L^1 \rangle$ moments to be related to the same bilinear expression in the $\pi\pi$ amplitudes T_l, within certain approximations.

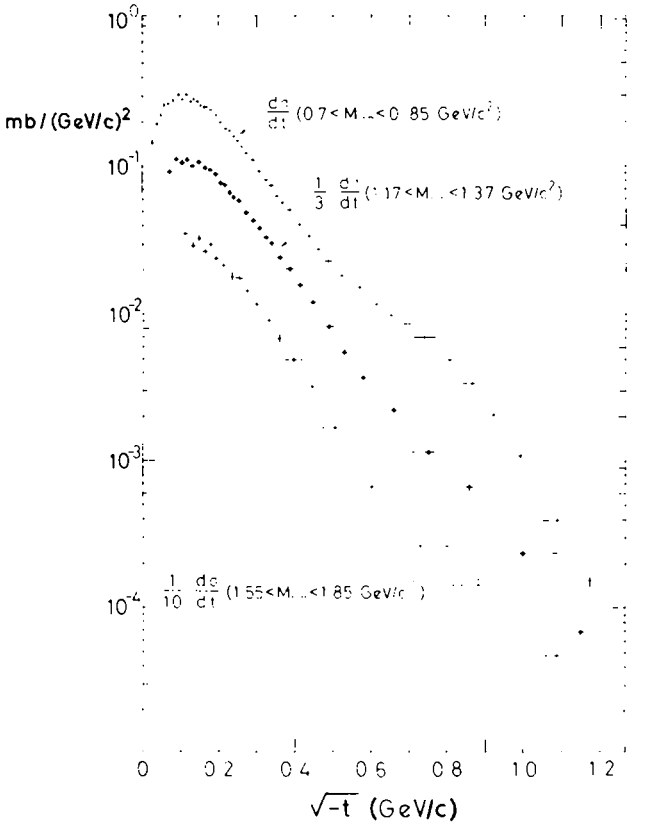

Fig. 20. Differential cross section as a function of $\sqrt{-t}$ for π-pair production in the ρ, f and g regions. $d\sigma/dt$, ρ region: 0.7 GeV/c^2 < $M_{\pi\pi}$ < 0.85 GeV/c^2 fit with L_{max} = 4, M_{max} = 2; $\frac{1}{3}d\sigma/dt$, f region: 1.17 GeV/c^2 < $M_{\pi\pi}$ < 1.37 GeV/c^2 fit with L_{max} = 5, M_{max} = 4; $\frac{1}{10}d\sigma/dt$, g region: 1.55 GeV/c^2 < $M_{\pi\pi}$ < 1.85 GeV/c^2 fit with L_{max} = 6, M_{max} = 4.

4.3. *Differential cross section* $d\sigma/dt$ *for* π*-pair production in the* ρ, f *and* g *regions*

In fig. 20 we have plotted the differential cross section $d\sigma/dt$ for $\pi^+\pi^-$ production in the ρ, f and g regions as a function of $\sqrt{-t}$. For the ρ region we chose the mass interval 0.7 GeV/c^2 < $M_{\pi\pi}$ < 0.85 GeV/c^2; for the f region 1.17 GeV/c^2 < $M_{\pi\pi}$ < 1.37 GeV/c^2; and for the g region 1.55 GeV/c^2 < $M_{\pi\pi}$ < 1.85 GeV/c^2. The dip of the cross section in the forward direction for $-t < \mu^2$, a typical feature of one-pion exchange in reaction (1), is rather pronounced in the ρ and f. For the g meson, values of $-t \leqslant \mu^2$ become unphysical. In all three curves, $d\sigma/dt$ is only given for $-t$ values larger than the minimum physical $|t|$ of the highest mass in the chosen $M_{\pi\pi}$ interval. The differential cross sections $d\sigma/dt$ for ρ, f and g production

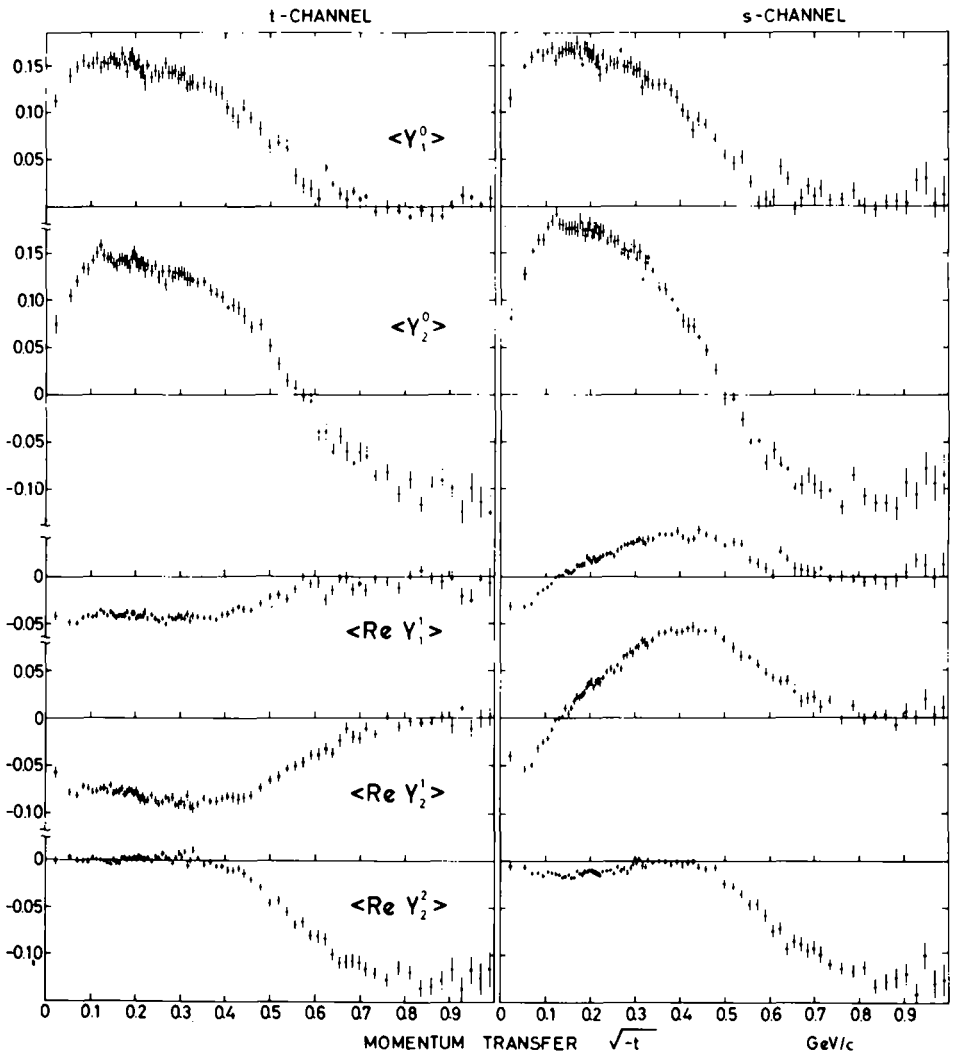

Fig. 21. t-dependence of $\langle Y_L^M \rangle$ in the ρ region ($0.71\ \text{GeV}/c^2 < M_{\pi\pi} < 0.83\ \text{GeV}/c^2$) obtained from fits with $L_{\max} = 2$, $M_{\max} = 2$ in the Gottfried–Jackson and s-channel helicity frames.

show nearly identical behaviour for $-t < 0.2\ (\text{GeV}/c^2$. At larger $|t|$ there are marked differences between the slopes of these three cross sections. All three slopes become flatter with increasing $|t|$, the largest effect being observed in the ρ. The differences in the slopes at large $|t|$ may be explained, as will be shown the next paragraphs, by different fractions of natural parity exchange in ρ, f and g production.

4.4. *t*-dependence of $\pi^+\pi^-$ angular distribution in the ρ-mass region and $\pi^+\pi^-$ production mechanism

Fig. 21 shows the t-dependence of the angular distribution moments for the Gottfried–Jackson frame in the ρ-mass region ($0.7\ \mathrm{GeV}/c^2 < M_{\pi\pi} < 0.85\ \mathrm{GeV}/c^2$). The usual spin density matrix elements $\rho^{l\,l_i}_{m_1 m_2}$ for a spin 0 and spin 1 mixture with the normalization $\rho^{00}_{00} + 2\rho^{11}_{11} + \rho^{11}_{00} = 1$, are related to the normalized moments $\langle Y^M_L \rangle$ as follows:

$$\begin{aligned}
&\mathrm{Re}\,\rho^{01}_{00} = \sqrt{4\pi}\tfrac{1}{2}\langle Y^0_1\rangle, && \mathrm{Re}\,\rho^{11}_{10} = \sqrt{4\pi}\sqrt{5/3}\tfrac{1}{2}\langle Y^1_2\rangle,\\
&\mathrm{Re}\,\rho^{01}_{01} = \sqrt{4\pi}\tfrac{1}{2}\langle Y^1_1\rangle, && \rho^{11}_{1-1} = -\sqrt{4\pi}\sqrt{5/6}\langle Y^2_2\rangle.\\
&\rho^{11}_{00} \quad \rho^{11}_{11} = \sqrt{4\pi}\sqrt{5}\tfrac{1}{2}\langle Y^0_2\rangle,
\end{aligned} \tag{32}$$

Corresponding relations for $l \leqslant 3$ are given in appendix A.

Defining the relative contributions of natural and unnatural parity exchange to the cross section for $\pi^+\pi^-$ production with helicity λ as $\rho^{\mathrm{n}}_\lambda$ and $\rho^{\mathrm{u}}_\lambda$, one obtains, in the Gottfried–Jackson frame, for the limit of large s, the relations [34]

$$\begin{aligned}
&\rho^{\mathrm{n}}_0 = 0, && \rho^{\mathrm{n}}_1 = \rho^{11}_{11} + \rho^{11}_{1-1},\\
&\rho^{\mathrm{u}}_0 = \rho^{00}_{00} + \rho^{11}_{00}, && \rho^{\mathrm{u}}_1 = \rho^{11}_{11} - \rho^{11}_{1-1}.
\end{aligned} \tag{33}$$

From relations (32) and (33) it can be seen that the contributions ρ^{u}_0, ρ^{u}_1 and ρ^{n}_1 cannot in general be determined from the observed angular distribution moments in a model-independent way; only upper and lower limits may be given. For instance, a lower limit for ρ^{u}_0 is given by the quantity

$$\rho^{11}_{00} + \tfrac{1}{3}\rho^{00}_{00} = \tfrac{1}{3} + \tfrac{1}{3}\sqrt{5(4\pi)}\langle Y^0_2\rangle,$$

which differs from ρ^{u}_0 only by $\frac{2}{3}\rho^{00}_{00}$. In fig. 22 we have compared the differential cross section $\mathrm{d}\sigma/\mathrm{d}t$ to the helicity zero combination $(\rho^{11}_{00} + \frac{1}{3}\rho^{00}_{00})\,\mathrm{d}\sigma/\mathrm{d}t$ which should project out the major contribution of π exchange. Fig. 22 shows that $\pi^+\pi^-$ production with helicity zero by unnatural parity exchange is the dominant contribution to the cross section at low $|t|$ values. At $|t|$ around 1 $(\mathrm{GeV}/c)^2$ however, the ρ meson is mainly produced in a state of helicity 1. Furthermore, one can derive from eqs. (32) and (33) that this state of helicity 1 is produced almost entirely by natural parity exchange, since $\rho^{11}_{1\,1}$ reaches almost its maximum possible value of $\frac{1}{2}$. From the data we find the limits $0.77 \leqslant \rho^{\mathrm{n}}_1 \leqslant 0.93$ at $-t \approx 1\ (\mathrm{GeV}/c)^2$.

A more complete picture of the relative contributions of natural and unnatural parity exchange may be obtained from an eigenvalue analysis of the spin density matrix which has been presented in a previous paper [8] for the spin 0 and 1 mixture in the ρ region. Since the imaginary parts of the density matrix and one diagonal

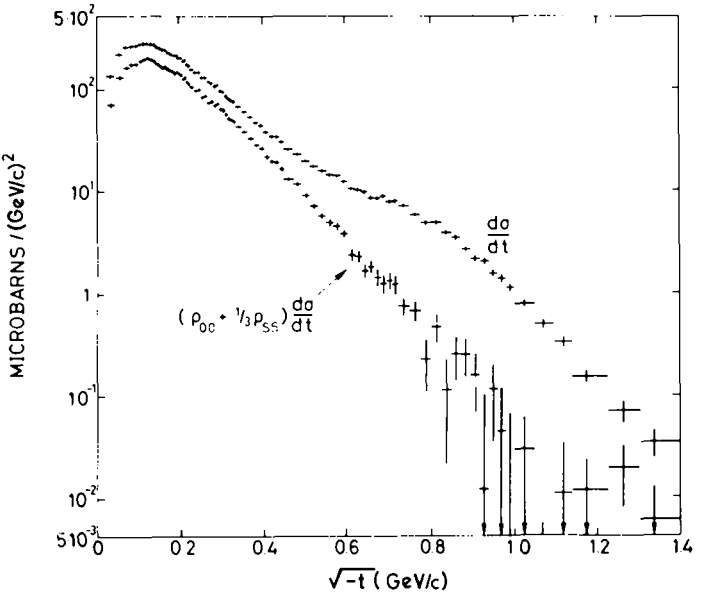

Fig. 22. t-channel helicity zero combination of differential cross section, $(\rho_{00}^{11} + \frac{1}{3}\rho_{00}^{00})\mathrm{d}\sigma/\mathrm{d}t$, in the ρ region ($0.71\ \mathrm{GeV}/c^2 < M_{\pi\pi} < 0.83\ \mathrm{GeV}/c^2$). $\mathrm{d}\sigma/\mathrm{d}t$ is also shown for comparison.

element are unknown, the eigenvalues cannot be determined exactly. However, the eigenvalues must lie within certain ranges for which the density matrix is positive definite for any value of the unmeasured elements. In practice, it turns out that in the ρ region those ranges of the eigenvalues are rather small so that a reasonably good determination of the eigenvalues is possible. From the four eigenvalues of the density matrix there is one corresponding to natural parity exchange only, and three eigenvalues corresponding to unnatural parity exchange. In fig. 23a we show the natural parity exchange eigenvalue x^n as a function of $\sqrt{-t}$; in fig. 23b the three eigenvalues of unnatural parity exchange. Of the latter, only x_1^u is of sizeable magnitude; x_2^u is very small, x_3^u has to be zero for theoretical reasons [8] and is shown here to be so experimentally. From fig. 23 it follows that the natural parity exchange contribution rises from $\sim 10\%$ at $-t \approx 0$ to $\sim 90\%$ at $-t \approx 1\ (\mathrm{GeV}/c)^2$.

We have made [5] a comparison between our data in the ρ region and the predictions of William's absorption model [33]. Such a comparison has been done previously with SLAC data at 15 GeV/c [35]. Williams' model, with equal form factors for the various helicity amplitudes, yields a parameter-free prediction for the moment ratios in the s-channel helicity frame. The experimental moment ratios in the s-channel helicity frame and the theoretical predictions for the ρ-mass region are plotted in fig. 24 as a function of t. They show remarkable agreement in the region $-t < 0.08\ (\mathrm{GeV}/c)^2$. Large deviations, however, appear at higher values of $-t$, especially in the ratio $\langle Y_2^1 \rangle / \langle Y_2^2 \rangle$ where the model apparently cannot explain

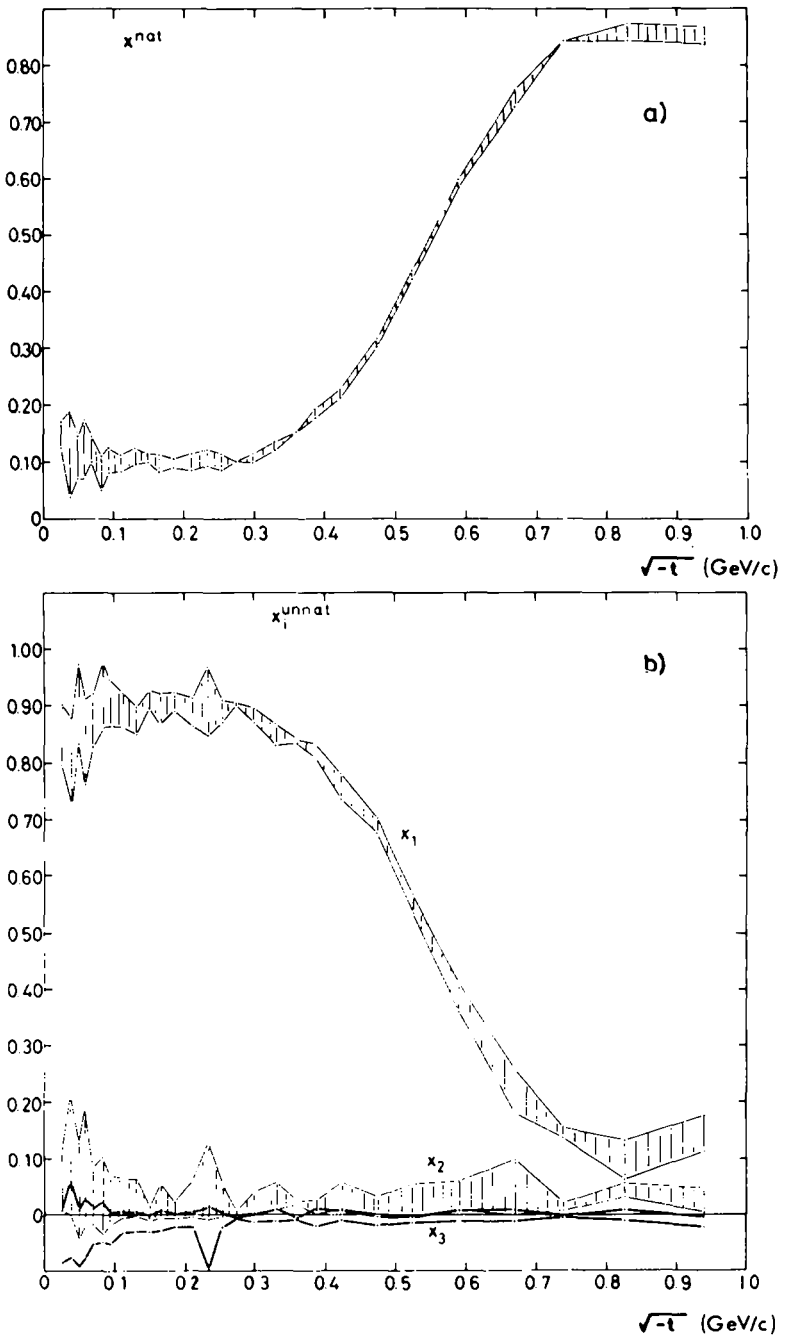

Fig. 23. Eigenvalues of the spin 0, 1 density matrix in the ρ region as a function of $\sqrt{-t}$: (a) the eigenvalue for natural parity exchange; (b) three eigenvalues for unnatural parity exchange.

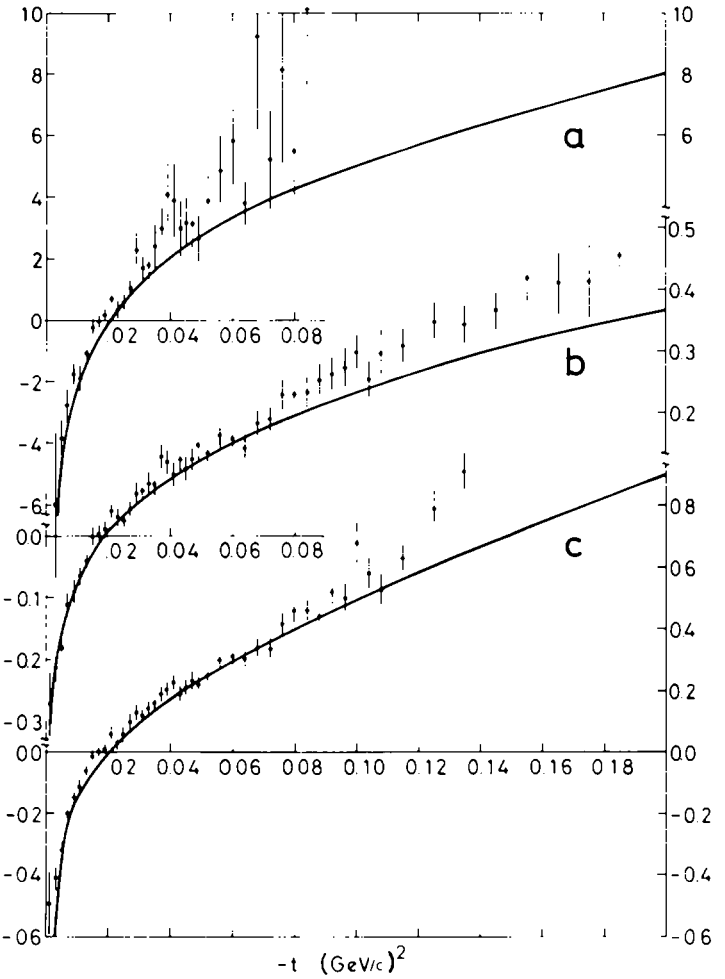

Fig. 24. Measured moment ratios in the s-channel helicity frame for the ρ region ($0.71\ \mathrm{GeV}/c^2 < M_{\pi\pi} < 0.83\ \mathrm{GeV}/c^2$) together with the absolute predictions of Williams' absorption model. (a) points $\langle Y_2^1\rangle/\langle Y_2^2\rangle$, curve predicted $(M/2\mu^2)(t+\mu^2)/\sqrt{-t}$; (b) points $\langle Y_1^1\rangle/\langle Y_1^0\rangle$, curve predicted $(1/\sqrt{2}M)(t+\mu^2)/\sqrt{-t}$; (c) points $\langle Y_2^1\rangle/\langle Y_2^0\rangle$, curve predicted $(\sqrt{3}M/\sqrt{2})\sqrt{-t}(t+\mu^2)/(t^2+M^2t+\mu^4)$.

the behaviour of the s-channel helicity Y_2^2 moment which reaches zero around $\sqrt{-t} = 0.3\ \mathrm{GeV}/c$ (fig. 21). Furthermore, when performing the model comparison in different mass bins over the ρ region, one finds deviations from the predicted curves changing systematically with $\pi^+\pi^-$ mass. The best agreement is in fact ob-

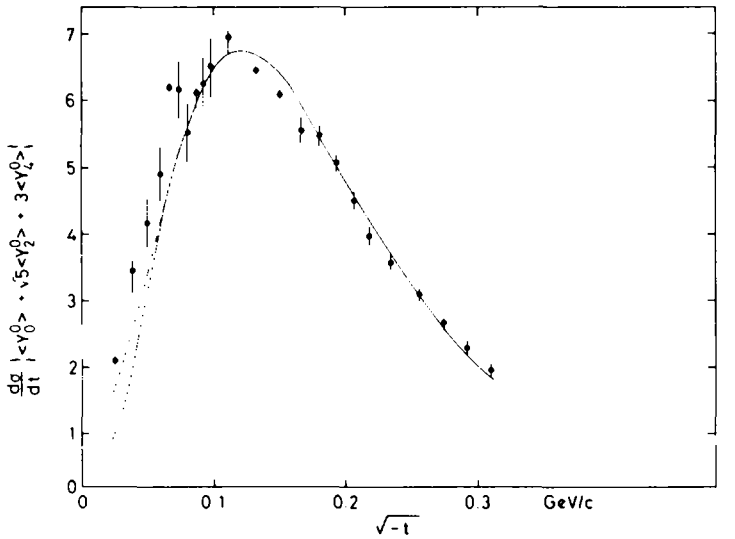

Fig. 25. Points with error bars give measurements of $(d\sigma/dt)\,(\langle Y_0^0\rangle + \sqrt{5}\langle Y_2^0\rangle + 3\langle Y_4^0\rangle$ *versus* $\sqrt{-t}$ for $700 < M_{\pi\pi} < 850$ MeV/c^2 ($d\sigma/dt$ in arbitrary units). The lower curve shows the function $-ct/(t-\mu^2)^2$ fitted to the data. The upper (dashed) curve shows a fit to the data of the same function with measurement errors folded in.

An examination of the data at $|t| \lesssim 0.003$ (GeV/c)^2 can give information about A_1 exchange. This would contribute helicity amplitudes with $m = 0$, but without nucleon spin flip. These, unlike π exchange, would not have to vanish at $t = 0$, and if present would show up at low $|t|$.

In fig. 25 for $700 < M_{\pi\pi} < 850$ MeV/c^2 we plot against $\sqrt{-t}$ the measured combination

$$\sqrt{4\pi}\,\frac{d\sigma}{dt}\{\langle Y_0^0\rangle + \sqrt{5}\langle Y_2^0\rangle + 3\langle Y_4^0\rangle\} = \frac{d\sigma}{dt}\{\rho_{00}^{00} + 3\rho_{00}^{11} + 5\rho_{00}^{22} + 2\sqrt{5}\rho_{00}^{20}\}\ ,$$

containing only $m = 0$ amplitudes.

Following the Williams model [33] we fit the expression

$$\frac{-ct\exp(At)}{(t-\mu^2)^2}$$

to the data (lower curve) with c, A fitted parameters. The upper curve is a fit of the same function, but with measurement errors folded in. There is a statistically significant excess of $m = 0$ intensity in the region $|t| < 0.005$ (GeV/c)^2. If our estimates of our resolution in t were wrong by a factor of 2, the effect would not be significant; however, we can find no reason to revise these estimates.

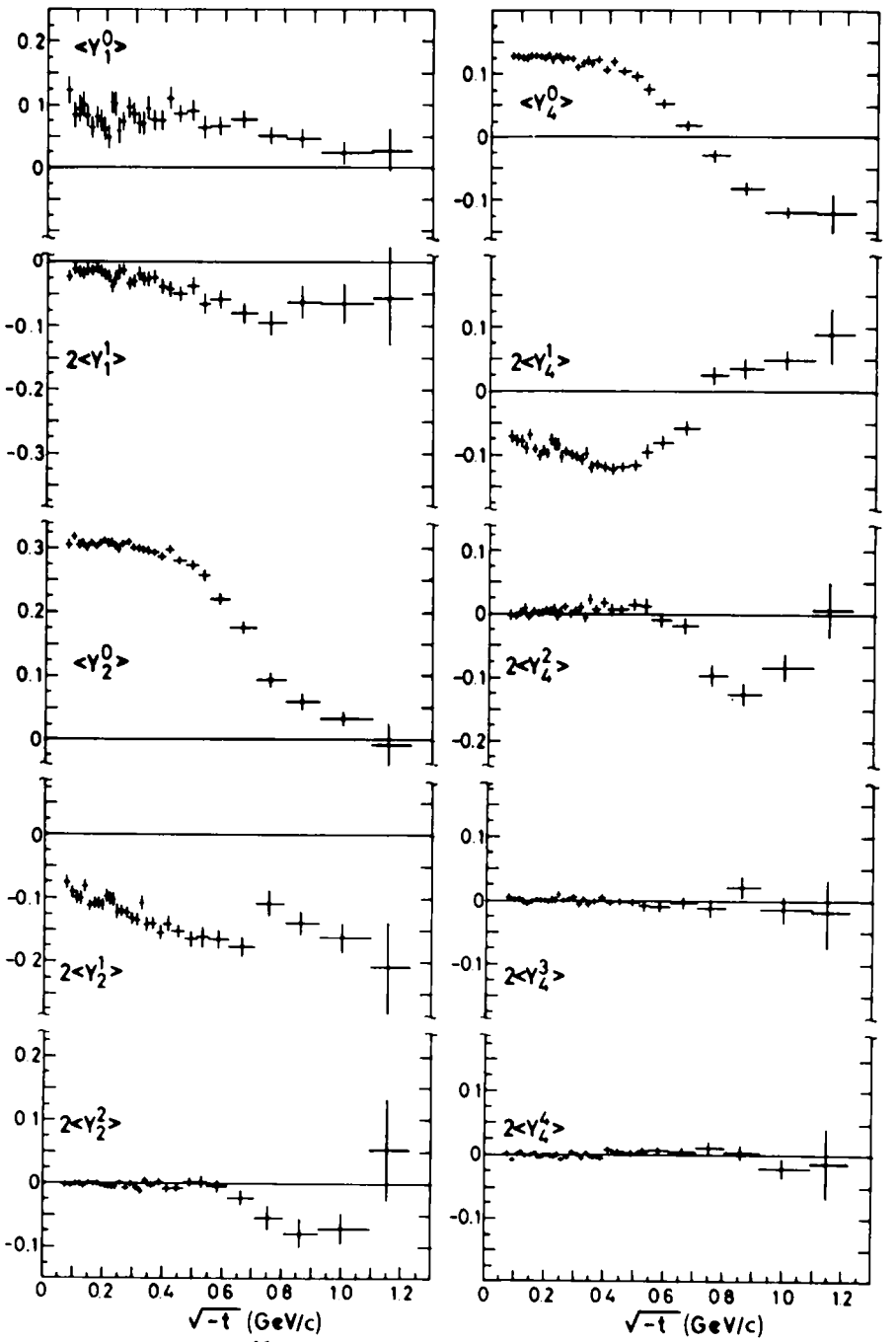

Fig. 26. t-dependence of $\langle Y_L^M \rangle$ in the f^0 region ($1.17\,\mathrm{GeV}/c^2 < M_{\pi\pi} < 1.37\,\mathrm{GeV}/c^2$) obtained from fits with $L_{max} = 5$, $M_{max} = 4$ in the Gottfried Jackson frame.

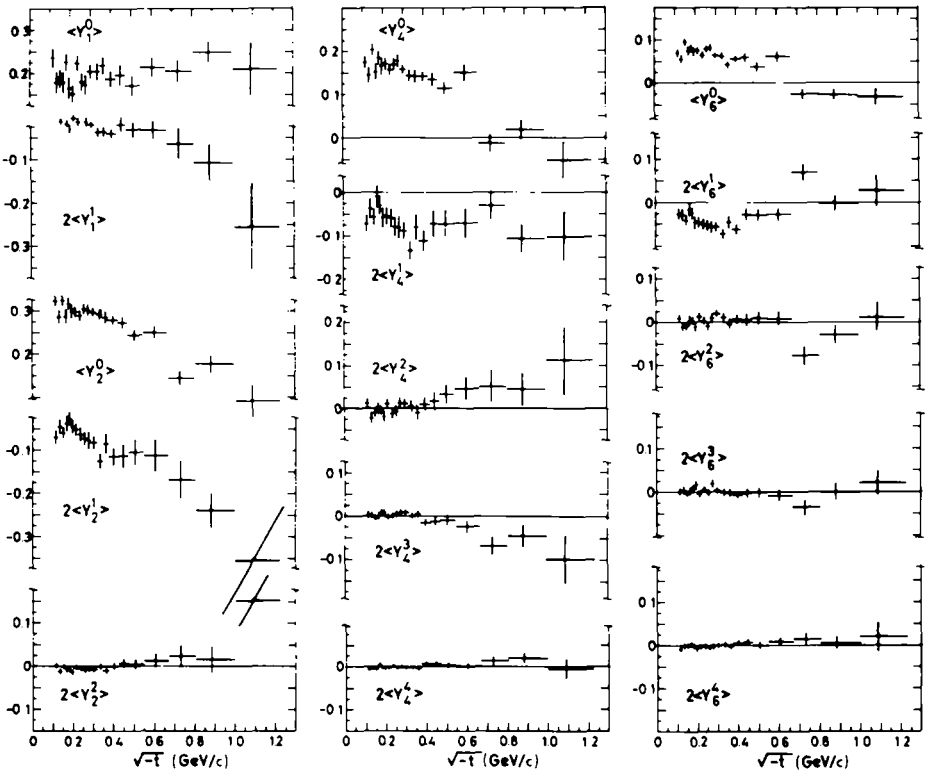

Fig. 27. t-dependence of $\langle Y_L^M \rangle$ in the g region ($1.55\,\mathrm{GeV}/c^2 < M_{\pi\pi} < 1.85\,\mathrm{GeV}/c^2$) obtained from fits with $L_{max} = 6$, $M_{max} = 4$ in the Gottfried Jackson frame.

4.5. *t-dependence of the $\pi^+\pi^-$ angular distribution in the f and g regions*

Figs. 26 and 27 display the angular distribution moments in the Gottfried Jackson frame as a function of $\sqrt{-t}$ for the f and g regions, respectively. We do not show the $L = 3$ and $L = 5$ moments, since they either cross zero at the resonance mass or vary rapidly over the resonance so that their average magnitude depends very much on the mass interval chosen. In the f region one may notice that $\langle Y_4^0 \rangle$, $\langle Y_4^1 \rangle$, and $\langle Y_4^2 \rangle$ show a behaviour rather similar to the corresponding $L = 2$ moments in the ρ region. In particular, from the large negative values of $\langle Y_4^0 \rangle$ and $\langle Y_4^2 \rangle$ at $-t \sim 1\ (\mathrm{GeV}/c)^2$, it follows that at large $|t|$, production by natural parity exchange in the t-channel helicity-one state is the dominant contribution to the cross section. From the $L = 4$ moments at $-t \sim 1\ \mathrm{GeV}^2$ we find as limits for natural parity exchange in f production

$$0.75 \geqslant (\rho_1^n = \rho_{11}^{22} + \rho_{1-1}^{22}) \geqslant 0.60 .$$

This result for the fraction ρ_1^n is smaller than the corresponding one for the ρ region. The relative decrease of the large t cross section with increasing $\pi\pi$ mass which we observed in fig. 20 may therefore be related to the decrease of the natural parity exchange contribution.

In the g-meson region (fig. 27) one finds again a certain analogy between the t-dependence of $\langle Y_6^0 \rangle$, $\langle Y_6^1 \rangle$, $\langle Y_6^2 \rangle$, and that of the corresponding moments in the f and ρ regions with $L = 4$ and $L = 2$, respectively. Also in g-meson production, natural parity exchange seems to become substantial at large $|t|$.

At small t the data may be diescribed again the by the poor man's absorption model [33]. The nucleon flip amplitude A_L^- for production of a $(\pi\pi)$ state with spin l, helicity $|m| = 1$ with unnatural parity exchange in the s-channel frame has a t-dependence:

$$A_L^- \sim \frac{2t}{t - \mu^2} - C_A \,.$$

The parameter C_A describes the absorptive correction to the pion exchange pole; $C_A = 1$ corresponds to the choice of the Williams' model in agreement with the data in the ρ region. A direct measure of C_A is provided by the position, t_0, of the zero of the moments $\langle Y_L^1 \rangle$, which are linearly related to the amplitudes A_L^- (one finds $C_A = -2t_0/(\mu^2 - t_0)$). Our measurement of the t-dependence of those moments is shown in figs. 28 and 29 for different $M_{\pi\pi}$ intervals. It is seen that while $\langle Y_L^1 \rangle$ vanishes at $t = -\mu^2$ ($C_A = 1$) for $M_{\pi\pi} \lesssim 800$ MeV/c^2, this zero clearly moves towards $t = 0$ with increasing $M_{\pi\pi}$. We have checked that the inclusion of nucleon non-flip amplitudes and of the amplitudes for helicity $m = 2$ production cannot change the position of the zero, t_0, by more than 2%.

The observed behaviour of the moments at our small t values is therefore a further piece of evidence for the effect that the strength of the absorptive correction (C_A) decreases with increasing mass, as has been pointed out recently [32,36].

4.6. Breit–Wigner fits to the f and g mesons

In principle the masses and widths of resonances are best determined by a phase-shift analysis, as discussed in subsect. 4.7. However, since this has not been, and indeed often could not be, done for most of the values reported in the literature, we give here the results of a rather direct determination of the "Breit–Wigner" parameters of the ρ, f and g mesons, as measured in this experiment. These have been obtained [37] by fitting Breit–Wigner forms to the distribution of the unnormalized moments $N\langle Y_{2l}^M \rangle$, $l = 1, 2, 3$, for $M = 0$ and 1. As already discussed in subsect. 4.2, such a procedure gives more reliable results than a fit to the mass spectrum, in which the form and magnitude of the non-resonant background in the resonance region are unknown. Only partial waves with angular momenta $l > 1$ ($l > 2, l > 3$) contribute background to the intensities fitted for the ρ (f, g) mesons by this method. From fig. 15 we see that these partial waves are negligible in these resonance regions.

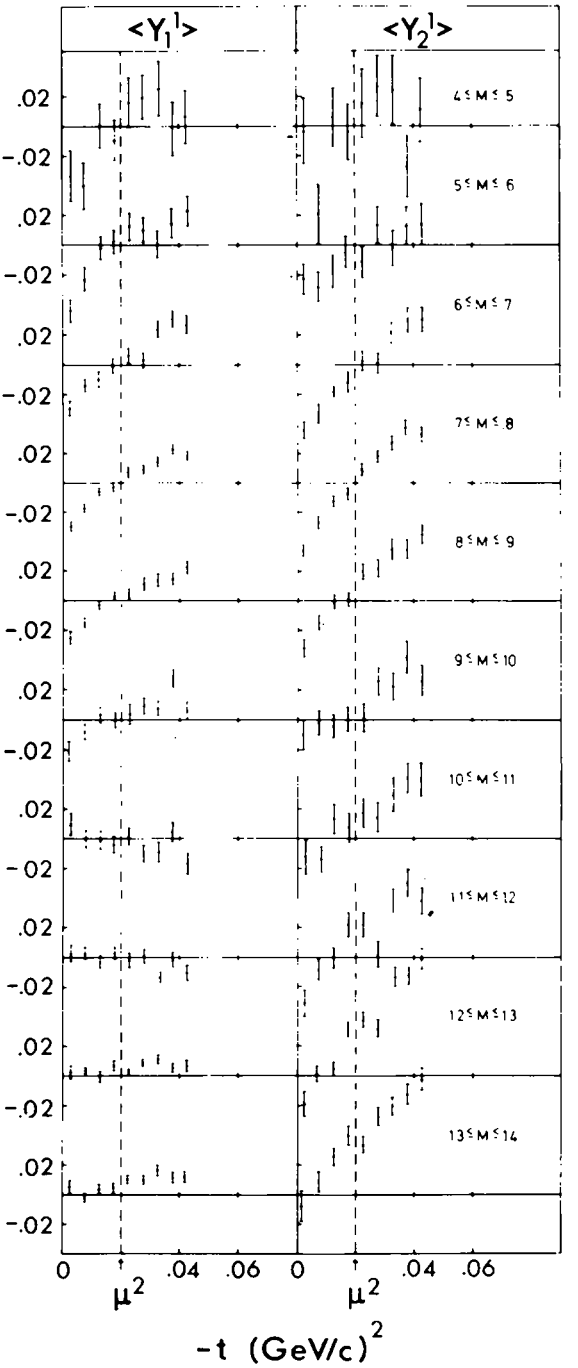

Fig. 28. $\langle Y_1^1 \rangle$ and $\langle Y_2^1 \rangle$ *versus* $|t|$ for a set of $M_{\pi\pi}$ intervals $0.4 < M < 1.4$ GeV/c^2

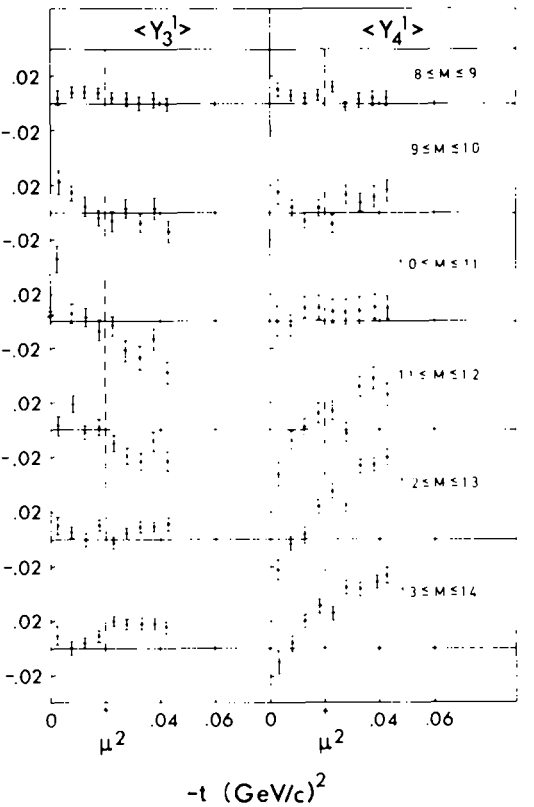

Fig. 29. $\langle Y_3^1 \rangle$ and $\langle Y_4^1 \rangle$ *versus* $|t|$ for a set of $M_{\pi\pi}$ intervals $0.8 < M < 1.4$ GeV/c^2.

For the fits we used the usual "relativistic" Breit–Wigner form, modified by the energy dependence of the Chew–Low equation to correct for the off-mass-shell pion [38]:

$$\frac{\mathrm{d}\sigma}{\mathrm{d}E} \propto \frac{E^2}{q} \frac{E_0^2 \Gamma^2}{(E^2 - E_0^2)^2 + E_0^2 \Gamma^2}, \tag{34}$$

with the energy dependence of Γ given by [39]

$$\Gamma = \Gamma_0 \left(\frac{q}{q_0}\right)^{2l+1} \frac{D_l(q_0 R)}{D_l(qR)}. \tag{35}$$

In these formulae E is the c.m. energy of the excited dipion state, q the c.m. momentum of each of the decay pions, l the resonance angular momentum; R is the range parameter, and D_l are angular momentum barrier penetration factors. E_0

Table 3
Results of fits of a Breit–Wigner expression for the ρ meson

Quantity fitted	t range $(GeV/c)^2$	E_ρ (MeV)	Γ_ρ (MeV)	R_ρ $(GeV/c)^{-1}$	χ^2	NDF	χ^2NDF
Y_2^0	0 – 0.15	778 ± 2	163 ± 4	2.8 ± 0.4	19.60	13	1.51
Y_2^1	0 – 0.15	763 ± 1	156 ± 3	27 $\sim\infty$	19.37	13	1.49
I_2	0 – 0.15	771 ± 1	161 ± 4	$12.1^{+2.0}_{-3.6}$	18.08	13	1.39
I_2^0	0 – 0.15	775 ± 2	163 ± 4	$4.5^{+0.8}_{-0.6}$	16.79	13	1.29
phase-shift analysis B	0.01 – 0.15	778 ± 2	152 ± 2	4.5 ± 0.4			

Table 4
Results of fits of a Breit–Wigner expression for the f meson

Quantity fitted	t range $(GeV/c)^2$	E_f (MeV)	Γ_f (MeV)	R_f $(GeV/c)^{-1}$	χ^2	NDF	χ^2NDF
Y_4^0	0.005 – 0.15	1273 ± 3	183 ± 3	5.4 ± 1.3	41.61	21	1.98
Y_4^1	0.005 – 0.15	1235 ± 4	180 ± 11	6.7 $\sim\infty$	12.69	21	0.62
I_4	0.005 – 0.15	1258 ± 4	192 ± 9	$10.1^{+\infty}_{-4.2}$	23.02	21	1.15
I_4^0	0.005 – 0.15	1267 ± 4	187 ± 8	$7.1^{+\infty}_{-1.9}$	29.55	21	1.48
Y_4^0	0.005 – 0.07	1269 ± 4	181 ± 9	5.1 ± 1.5	38.12	21	1.82
Y_4^1	0.005 – 0.07	1228 ± 5	167 ± 13	6.1 $\sim\infty$	27.19	21	1.30
I_4	0.005 – 0.07	1255 ± 4	187 ± 11	$8.8^{+\infty}_{-2.6}$	35.59	21	1.65
I_4^0	0.005 – 0.07	1264 ± 5	185 ± 11	$6.7^{+\infty}_{-1.9}$	31.48	21	1.50
Y_4^0	0.07 – 0.4	1272 ± 5	156 ± 9	$3.6^{+0.9}_{-0.6}$	35.02	21	1.67
Y_4^1	0.07 – 0.4	1247 ± 5	196 ± 14	7.4 $\sim\infty$	30.68	21	1.46
I_4	0.07 – 0.4	1261 ± 4	188 ± 10	9.1 $\sim\infty$	28.26	21	1.35
I_4^0	0.07 – 0.4	1267 ± 5	172 ± 9	$5.1^{+2.3}_{-1.0}$	34.37	21	1.64
phase-shift analysis B	0.01 – 0.15	1279 ± 3	202 ± 6	5.3 ± 1.2			

Table 5
Results of fits of a Breit–Wigner expression for the g meson

Quantity fitted	t range $(GeV/c)^2$	E_g (MeV)	Γ_g (MeV)	R_g $(GeV/c)^{-1}$	χ^2	NDF	χ^2NDF
Y_6^0	0.015 – 0.15	1703 ± 5	190 ± 13	4.9 $\sim\infty$	18.15	18	1.01
Y_6^1	0.015 – 0.15	1674 ± 9	188 ± 29	4.9 $\sim\infty$	16.52	18	0.92
I_6	0.015 – 0.15	1693 ± 8	200 ± 18	$9.1^{+\infty}_{-4.7}$	10.58	18	0.59
I_6^0	0.015 – 0.15	1696 ± 5	182 ± 12	8.5 $\sim\infty$	25.10	18	1.40
phase-shift analysis B	0.01 – 0.15	1713 ± 4	228 ± 10	6.4 ± 4			

denotes the resonant energy, Γ_0 the width of the resonance, and q_0 the momentum of a decay pion at resonance. The parameters E_0, Γ_0, and R were fitted by a least squares method. Details of the fitting procedure will be given elsewhere [37]. The results for the ρ, f, and g mesons are summarized in tables 3, 4 and 5, respectively. These tables also give the values of E_0, Γ_0 and R determined by a phase-shift analysis of the same data (see subsect. 4.7.2 below).

It is seen that the resonant energies E_0 from the fits to $N\langle Y_{2l}^0\rangle$ are consistently higher than those from $N\langle Y_{2l}^1\rangle$; this is a consequence of the increase of the ratio $|\langle Y_L^0\rangle/\langle Y_L^1\rangle|$ with increasing mass, as shown in fig. 19. This exposes the disadvantage of fitting these individual moments, namely that they project out only part of the intensity of the resonant wave, and this fraction changes over the resonance. However, it is possible to project out the full intensity of the resonant wave under the assumption that one-pion exchange with absorption is the dominant production mechanism. From this it may be shown [10] that in the t range considered, only s-channel nucleon helicity flip amplitudes are present, and that these amplitudes are relatively real for a given spin l of the $\pi\pi$ system. These assumptions have been confirmed experimentally in the ρ meson region [8], and are supported by the evidence at higher masses. In the t-channel, all moments $\langle Y_L^M\rangle$ with $M > 1$ are zero within the t interval considered, which together with the above assumptions results in simple relations between the $M = 0$ and 1 moments and the relevant helicity amplitudes f_l^m (which all correspond to nucleon helicity flip in the s-channel):

$$N\langle Y_{2l}^0\rangle = \alpha_l (f_l^0)^2 + \beta_l (f_l^1)^2 , \qquad N\langle Y_{2l}^1\rangle = \gamma_l f_l^0 f_l^1 .$$

These equations may be solved [37] for the real amplitudes f_l^0 and f_l^1, which yield the total intensity of the spin l partial waves:

$$I_{2l} = I_{2l}^0 + I_{2l}^1 = (f_l^0)^2 + (f_l^1)^2 .$$

The results of fits of the Breit–Wigner expression (34) to the partial wave intensities I_{2l} are also given in tables 3–5, and the calculated intensities together with the fitted curves are displayed in fig. 30. In addition, results of fits to only the helicity zero part of the intensities (I_L^0) are given, since it may be argued that these represent the "real" resonances, undistorted by the effects of absorption.

The values of our parameters are generally compatible with the world average values [24]. For the ρ meson, for which many high statistics samples exist, our results clearly show the large differences between the various distributions examined. The t range chosen for the fits was such as to exclude any significant effect from ρ–ω interference. In the case of the f meson, there are even large discrepancies in the reported widths; in fact, the distribution is double-peaked [24] around 130 and 175 MeV. In order to investigate a possible t-dependence of the width which might give rise to this difference, the data were also divided into two t bins which were fitted separately (table 4). No significant difference was found, our results clearly

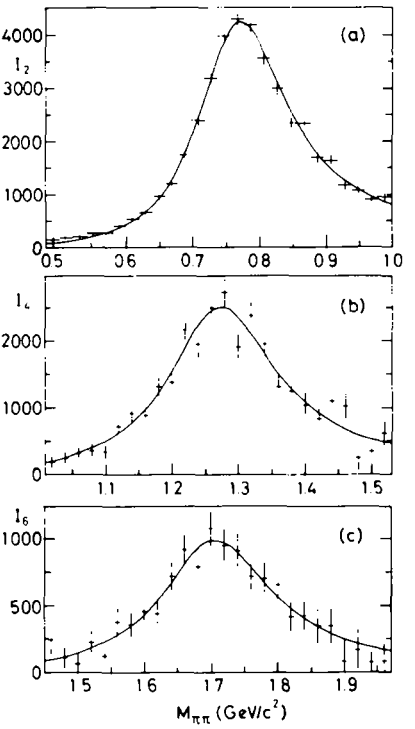

Fig. 30. $\pi^+\pi^-$ intensities (a) I_2 (l = 1) (b) I_4(l = 2) (c) I_6 (l = 3) in the ρ, f, g resonance regions. The curves are Breit-Wigner fits.

favouring the larger value. For the g meson, agreement is good, but the data-table values are strongly pulled away from our values by one experiment of Matthews et al. [40], which gives both a mass and width statistically well below the average.

4.7. $\pi\pi$ phase shifts

In this section we mention briefly the results of a number of $\pi\pi$ scattering phase-shift analyses which have been performed on our data. In fig. 31 we compare the resulting I = 0 S-wave phase shifts, obtained from these analyses, with one another and with those found by Protopopescu et al. [28] from the reaction $\pi^- p \to \Delta^{++}\pi^+\pi^-$ at 7.1 GeV/c.

4.7.1. (A) Pole extrapolation in $M_{\pi\pi}$ range 500–1500 MeV/c^2

An analysis has been carried out in the $\pi\pi$-mass region between 0.5 GeV/c^2 and 1.5 GeV/c^2. An account of the procedure has been given in a conference report [4]. In this analysis the on-shell $\pi\pi$ scattering cross section to which the phase shifts were fitted was obtained by extrapolating the observed t-channel helicity moments

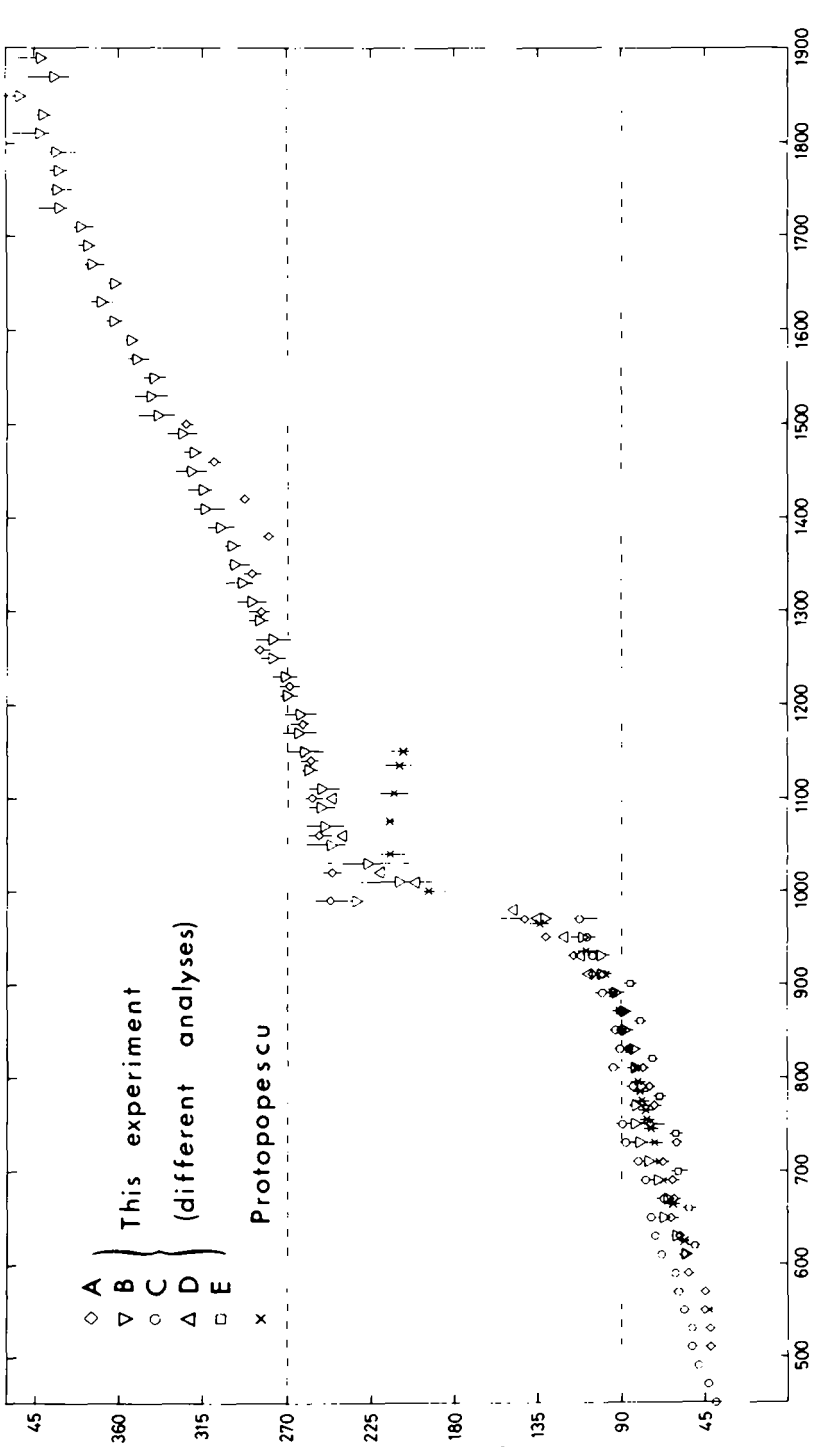

Fig. 31. The $\pi\pi$ scattering phase shift δ_0^0 for spin 0 and isospin 0 as determined by various analyses of our 17 GeV/c $\pi^+\pi^-$ data (A,B,C,D,E), compared with the previous results by Protopopescu et al. [28]: (A) Analysis based on pole extrapolations of the moments (subsect. 4.7.1. (A)). (B) Analysis at each $m_{\pi\pi}$ with $\pi^+\pi^-$ amplitudes assumed to be nucleon-spin and $\pi\pi$-spin coherent, involving a parametrization to describe the $m_{\pi\pi}$ dependence (subsect. 4.7.2. (B)). (C) Analysis at each $m_{\pi\pi}$ with $\pi^+\pi^-$ amplitudes assumed to be nucleon-spin coherent and using absorption corrections (subsect. 4.7.3. (C)). (D) Analysis with a constant K-matrix fit using $\pi^+\pi^-$ and K^+K^-n data simultaneously (subsect. 4.7.4 (D)). (E) Analysis with $\pi^+\pi^-$ amplitudes assumed to be $\pi\pi$-spin coherent and using the ρ-meson line shape (subsect. 4.7.5 (E)).

with $M = 0$ to the pion pole, using the Chew - Low extrapolation formula multiplied by a Dürr- Pilkuhn form factor and by a second-order polynomial in t. As further constraints for the phase shifts in some of the fits, expressions for the t-dependence of the $M = 1$ moments were also used. These have been derived by Froggatt and Morgan in a study of the kinematic singularities for the considered reaction [41]. The mass-dependence of the phase shifts was not parametrized, i.e. an energy-independent phase-shift analysis was performed yielding one (or several ambiguous) phase-shift values for every $\pi\pi$-mass bin.

The resulting $I = 0$ S-wave phase shift is shown in fig. 31. In the mass range 700 900 MeV/c^2, two S-wave solutions were found (the "up-down" ambiguity). However above 900 MeV/c^2 the "up" branch did not yield a solution, and could thus be ruled out.

4.7.2. (B) Parametrization in $M_{\pi\pi}$ range 600- 1900 MeV/c^2

A mass dependent and a mass independent analysis have been carried out in the $\pi\pi$-mass range 600–1900 MeV/c^2. The work is described in detail elsewhere [10]. The basic assumptions of this analysis are that s-channel helicity amplitudes with nucleon flip dominate; that helicity amplitudes for production of a $\pi\pi$ system with spin l are in phase for each natural and unnatural exchange amplitude separately; and that the relative phase between natural and unnatural exchange amplitudes is independent of l.

This analysis has led to a fairly satisfactory parametrization of the moments shown in figs. 14 and 15. The resulting S-wave $I = 0$ phase shifts are shown in fig. 31. Fig. 32 shows the Argand diagrams for the S-, P-, D- and F-wave amplitudes. The χ^2 for the fit is considerably improved by including a spin 1 resonance whose mass, width, and elasticity are determined to be 1590 ± 20 MeV/c^2, and 0.25 respectively. The resonance parameters determined for the ρ, f and g mesons are given in tables 3, 4 and 5.

4.7.3. (C) Mass-independent fit in $M_{\pi\pi}$ range 440–1400 MeV/c^2

This amplitude analysis [13] has been carried out both by using the one postulate that there is only π unnatural parity exchange (no A_1 exchange), and also by adding the constraint that the different P-wave helicity states are in phase. These two analyses give consistent results. The preferred S-wave solution from this analysis is shown in fig. 31.

4.7.4. (D) Coupled channel analysis in $M_{\pi\pi}$ range 900 1120 MeV/c^2

An energy-dependent phase-shift analysis has been carried out [12] using not only the data of reaction (1) from this experiment, but also data from our measurements [11] of the reactions

$$\pi^+ p \to \pi^+ \pi^+ n$$

for the $I = 2$ scattering, and our measurements [12] of

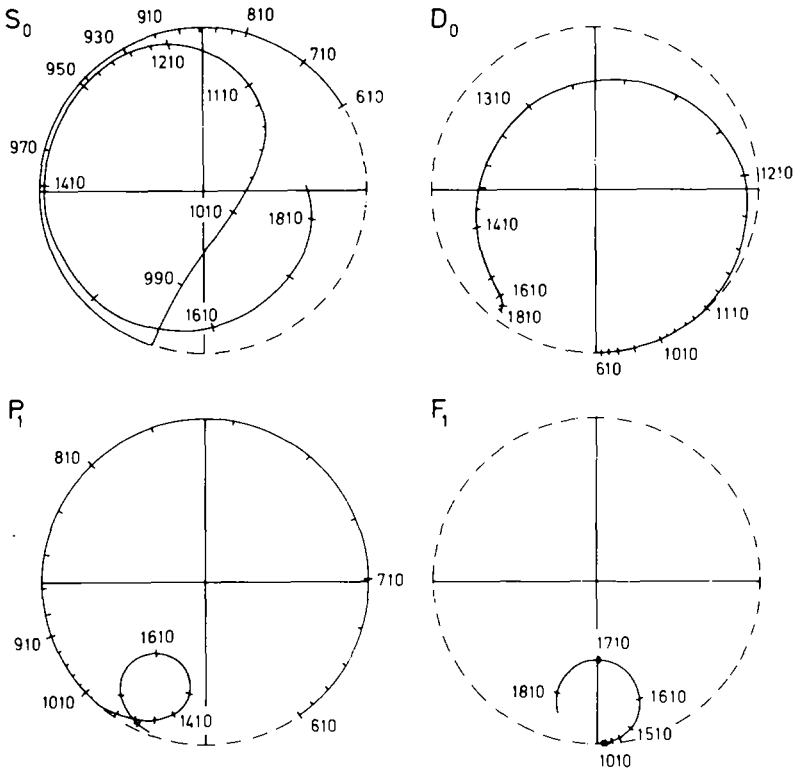

Fig. 32. Argand diagrams (Im T_l^I *versus* Re T_l^I) for the partial-wave amplitudes from the energy-dependent fit. Numbers indicate the $\pi\pi$ mass in MeV/c^2.

$$\pi^- p \to K^+ K^- n$$

to include a direct mesurement of the contribution from the main inelastic amplitude. The S-wave phase shift resulting from this analysis is shown in fig. 31.

4.7.5. (E) Mass-dependent fit in $M_{\pi\pi}$ range 600–920 MeV/c^2

A mass-dependent amplitude analysis in the $\pi\pi$-mass range 600–920 MeV/c^2 has been carried out [9], assuming the P-wave to be given by a Breit–Wigner function, and assuming the different M-states to be in phase. The resulting S-wave $\pi\pi$ phase shift is shown in fig. 31.

4.7.6. Discussion of results

The various analyses of the data from this experiment and that of Protopopescu et al. [28] all agree qualitatively for the S-wave $I = 0$ phase shift. In particular they

Table 6
S^* parameters

Analysis	Mass (MeV/c^2)	$\Gamma = 2\,\mathrm{Im}E_0$ (MeV/c^2)
This experiment B (ref. [10])	1007 ± 20	30 ± 10
This experiment C (ref. [13])	997	10
This experiment D (ref. [12])	1012 ± 6	32 ± 10
Protopopescu et al.(ref. [28])	997 ± 5	54 ± 16

all choose the solution shown in fig. 31 and not the alternative ambiguous phase shift around 800–900 MeV/c^2. This choice is compatible with recent data on $\pi^0\pi^0$ production [42,13]. A consequence of this choice has been to rule out an earlier suggestion [43] that the best set of amplitudes describing reaction (1) required a phase between different helicity P-wave amplitudes.

We confirm with good statistical significance that the S-wave passes through resonance (270°) around $M_{\pi\pi} = 1.25$ GeV/c^2, as has been pointed out by Beaupre et al. [44] and Carrol et al. [45].

The S-wave inelasticity at $K\bar{K}$ threshold requires some virtual bound state above, or resonance below, threshold. Table 6 gives the parameters determined for this state by three analyses of our data [10,12,13] and that of Protopopescu et al. [28]. These determinations are consistent within their quoted errors.

In the range 1020–1120 MeV/c^2 our S-wave phase shifts are clearly incompatible with those found by Protopopescu et al. [28]. This arises from different choices among ambiguous solutions, and it is not yet clear whether either one can be ruled out decisively.

$\pi\pi$ scattering phase shifts have been determined by measuring different reactions, for example $\pi^+ p \to \Delta^{++}\pi^+\pi^-$ [28] as well as reaction (1). In a given reaction they have been determined for widely varying total reaction energy. The resulting phase shifts are strikingly similar. In this experiment our analysis of subsect. 4.7.2 has found plausible, though not yet compelling, evidence for a ρ' meson ($J^P = 1^-$) at mass around 1600 MeV/c^2. This result, like the phase shift behaviour at $K\bar{K}$ threshold, shows elastic phase-shift behaviour related to processes occurring in inelastic $\pi\pi$ scattering. The over-all consistency gives support to the conclusion that the analysis of $\pi\pi$ scattering is approaching the precision that has been achieved in our knowledge of π-nucleon scattering.

We would like to thank Professor J. Heisenberg for his work in the early stage of preparing the experiment, Dr. G. Lutz for valuable discussions, Mrs. C. Ponting and Miss G. Waltermann for their assistance in our data processing, and Messrs. L. Bonet, L. Hubbeling, W. Mayr and M. Poeschel for their contributions to the construction of the apparatus.

Appendix

We give here the relationships between the spherical harmonics $\langle Y_L^M \rangle$ of the $\pi\pi$ angular distribution and the spin density matrix elements $\rho^{L_1 L_2}_{M_1 M_2}$ for $L \leqslant 3$.

$\sqrt{4\pi}\langle Y_0^0\rangle \equiv 1$	$+1.000\,\rho_{00}^{00}$	$+1.000\,\rho_{00}^{11}$	$+2.000\,\rho_{11}^{11}$	$+1.000\,\rho_{00}^{22}$
	$+2.000\,\rho_{11}^{22}$	$+2.000\,\rho_{22}^{22}$	$+1.000\,\rho_{00}^{33}$	$+2.000\,\rho_{11}^{33}$
	$+2.000\,\rho_{22}^{33}$	$+2.000\,\rho_{33}^{33}$		
$\sqrt{4\pi}\langle Y_1^0\rangle$	$+2.000\,\rho_{00}^{10}$	$+1.789\,\rho_{00}^{21}$	$+3.098\,\rho_{11}^{21}$	$+1.757\,\rho_{00}^{32}$
	$+3.312\,\rho_{11}^{32}$	$+2.619\,\rho_{22}^{32}$		
$\sqrt{4\pi}\langle \mathrm{Re}\, Y_1^1\rangle$	$+2.000\,\rho_{10}^{10}$	$-0.894\,\rho_{01}^{21}$	$+1.549\,\rho_{10}^{21}$	$+2.191\,\rho_{21}^{21}$
	$-1.014\,\rho_{01}^{32}$	$+1.434\,\rho_{10}^{32}$	$-0.586\,\rho_{12}^{32}$	$+1.852\,\rho_{21}^{32}$
	$+2.268\,\rho_{32}^{32}$			
$\sqrt{4\pi}\langle Y_2^0\rangle$	$+0.894\,\rho_{00}^{11}$	$-0.894\,\rho_{11}^{11}$	$+2.000\,\rho_{00}^{20}$	$+0.639\,\rho_{00}^{22}$
	$+0.639\,\rho_{11}^{22}$	$-1.278\,\rho_{22}^{22}$	$+1.757\,\rho_{00}^{31}$	$+0.596\,\rho_{00}^{33}$
	$+2.869\,\rho_{11}^{31}$	$+0.894\,\rho_{11}^{33}$	$-1.491\,\rho_{33}^{33}$	
$\sqrt{4\pi}\langle \mathrm{Re}\, Y_2^1\rangle$	$+1.549\,\rho_{10}^{11}$	$+2.000\,\rho_{10}^{20}$	$+0.639\,\rho_{10}^{22}$	$+1.565\,\rho_{21}^{22}$
	$-1.014\,\rho_{01}^{31}$	$+1.656\,\rho_{10}^{31}$	$+0.422\,\rho_{10}^{33}$	$+1.852\,\rho_{21}^{31}$
	$+1.155\,\rho_{21}^{33}$	$+1.491\,\rho_{32}^{33}$		
$\sqrt{4\pi}\langle \mathrm{Re}\, Y_2^2\rangle$	$-1.095\,\rho_{1\ 1}^{11}$	$-0.782\,\rho_{1-1}^{22}$	$+2.000\,\rho_{20}^{20}$	$-1.278\,\rho_{20}^{22}$
	$+0.586\,\rho_{1\ 1}^{31}$	$-0.730\,\rho_{1-1}^{33}$	$+1.309\,\rho_{20}^{31}$	$1.333\,\rho_{20}^{33}$
	$+2.268\,\rho_{31}^{31}$	$0.943\,\rho_{31}^{33}$		
$\sqrt{4\pi}\langle Y_3^0\rangle$	$+1.757\,\rho_{00}^{21}$	$-2.028\,\rho_{11}^{21}$	$+2.000\,\rho_{00}^{30}$	$+1.193\,\rho_{00}^{32}$
	$+0.843\,\rho_{11}^{32}$	$-2.667\,\rho_{22}^{32}$		
$\sqrt{4\pi}\langle \mathrm{Re}\, Y_3^1\rangle$	$+1.434\,\rho_{01}^{21}$	$+1.656\,\rho_{10}^{21}$	$-0.586\,\rho_{21}^{21}$	$+0.422\,\rho_{01}^{32}$
	$+2.000\,\rho_{10}^{30}$	$+0.894\,\rho_{10}^{32}$	$+1.461\,\rho_{12}^{32}$	$+1.155\,\rho_{21}^{32}$
	$-0.943\,\rho_{32}^{32}$			
$\sqrt{4\pi}\langle \mathrm{Re}\, Y_3^2\rangle$	$1.852\,\rho_{1\ 1}^{21}$	$+1.309\,\rho_{20}^{21}$	$1.333\,\rho_{02}^{32}$	$-1.155\,\rho_{1\ -1}^{32}$
	$+2.000\,\rho_{20}^{30}$	$+1.491\,\rho_{31}^{32}$		

$\sqrt{4\pi}\langle \mathrm{Re}\, Y_3^3 \rangle$	$2.268\,\rho_{2\ 1}^{21}$ $1.491\,\rho_{30}^{32}$	$0.943\,\rho_{1-2}^{32}$	$1.491\,\rho_{2\ 1}^{32}$	$+2.000\,\rho_{30}^{30}$
$\sqrt{4\pi}\langle Y_4^0 \rangle$	$+0.857\,\rho_{00}^{22}$ $+0.545\,\rho_{00}^{33}$ $+0.545\,\rho_{33}^{33}$	$1.143\,\rho_{11}^{22}$ $2.138\,\rho_{11}^{31}$	$+0.286\,\rho_{22}^{22}$ $+0.182\,\rho_{11}^{33}$	$+1.746\,\rho_{00}^{31}$ $-1.273\,\rho_{22}^{33}$
$\sqrt{4\pi}\langle \mathrm{Re}\, Y_4^1 \rangle$	$+1.565\,\rho_{10}^{22}$ $+0.704\,\rho_{10}^{33}$	$0.639\,\rho_{21}^{22}$ $0.756\,\rho_{21}^{31}$	$+1.380\,\rho_{01}^{31}$ $+1.029\,\rho_{21}^{33}$	$+1.690\,\rho_{10}^{31}$ $-0.996\,\rho_{32}^{33}$
$\sqrt{4\pi}\langle \mathrm{Re}\, Y_4^2 \rangle$	$-0.904\,\rho_{1\ 1}^{22}$ $+1.512\,\rho_{20}^{31}$	$+1.107\,\rho_{20}^{22}$ $-0.315\,\rho_{20}^{33}$	$-1.690\,\rho_{1\ 1}^{31}$ $0.436\,\rho_{31}^{31}$	$-0.575\,\rho_{1\ 1}^{33}$ $+1.336\,\rho_{31}^{33}$
$\sqrt{4\pi}\langle \mathrm{Re}\, Y_4^3 \rangle$	$1.690\,\rho_{2\ 1}^{22}$ $-1.443\,\rho_{30}^{33}$	$2.000\,\rho_{2\ 1}^{31}$	$0.680\,\rho_{2\ 1}^{33}$	$+1.155\,\rho_{30}^{31}$
$\sqrt{4\pi}\langle \mathrm{Re}\, Y_4^4 \rangle$	$+1.195\,\rho_{2-2}^{22}$	$+0.761\,\rho_{2\ 2}^{33}$	$2.309\,\rho_{3\ 1}^{31}$	$+1.178\,\rho_{3-1}^{33}$
$\sqrt{4\pi}\langle Y_5^0 \rangle$	$+1.699\,\rho_{00}^{32}$	$-2.402\,\rho_{11}^{32}$	$+0.760\,\rho_{22}^{32}$	
$\sqrt{4\pi}\langle \mathrm{Re}\, Y_5^1 \rangle$	$+1.519\,\rho_{01}^{32}$ $+0.170\,\rho_{32}^{32}$	$+1.612\,\rho_{10}^{32}$	$0.658\,\rho_{12}^{32}$	$0.832\,\rho_{21}^{32}$
$\sqrt{4\pi}\langle \mathrm{Re}\, Y_5^2 \rangle$	$+1.005\,\rho_{02}^{32}$	$-1.741\,\rho_{1-1}^{32}$	$+1.348\,\rho_{20}^{32}$	$-0.449\,\rho_{31}^{32}$
$\sqrt{4\pi}\langle \mathrm{Re}\, Y_5^3 \rangle$	$+1.421\,\rho_{1\ 2}^{32}$	$1.798\,\rho_{2\ 1}^{32}$	$+0.899\,\rho_{30}^{32}$	
$\sqrt{4\pi}\langle \mathrm{Re}\, Y_5^4 \rangle$	$+1.907\,\rho_{2\ 2}^{32}$	$-1.557\,\rho_{3-1}^{32}$		
$\sqrt{4\pi}\langle \mathrm{Re}\, Y_5^5 \rangle$	$+2.462\,\rho_{3\ 2}^{32}$			
$\sqrt{4\pi}\langle Y_6^0 \rangle$	$+0.840\,\rho_{00}^{33}$	$1.261\,\rho_{11}^{33}$	$+0.504\,\rho_{22}^{33}$	$0.084\,\rho_{33}^{33}$
$\sqrt{4\pi}\langle \mathrm{Re}\, Y_6^1 \rangle$	$+1.572\,\rho_{10}^{33}$	$-0.861\,\rho_{21}^{33}$	$+0.222\,\rho_{32}^{33}$	
$\sqrt{4\pi}\langle \mathrm{Re}\, Y_6^2 \rangle$	$0.861\,\rho_{1\ 1}^{33}$	$+1.258\,\rho_{20}^{33}$	$0.445\,\rho_{31}^{33}$	
$\sqrt{4\pi}\langle \mathrm{Re}\, Y_6^3 \rangle$	$1.634\,\rho_{2\ 1}^{33}$	$+0.770\,\rho_{30}^{33}$		
$\sqrt{4\pi}\langle \mathrm{Re}\, Y_6^4 \rangle$	$+0.943\,\rho_{2\ 2}^{33}$	$1.218\,\rho_{3-1}^{33}$		

$\sqrt{4\pi}\langle \mathrm{Re}\, Y_6^5 \rangle$	$+1.806\, \rho_{3\ 2}^{33}$
$\sqrt{4\pi}\langle \mathrm{Re}\, Y_6^6 \rangle$	$-1.277\, \rho_{3\ 3}^{33}$

References

[1] G. Grayer, B. Hyams, C. Jones, P. Schlein, W. Blum, H. Dietl, W. Koch, H. Lippmann, E. Lorenz, G. Lütjens, W. Männer, J. Meissburger, U. Stierlin and P. Weilhammer, Phys. Letters 34B (1971) 333.

[2] G. Grayer, B. Hyams, C. Jones, P. Schlein, W. Blum, H. Dietl, W. Koch, H. Lippmann, E. Lorenz, G. Lütjens, W. Männer, J. Meissburger, W. Ochs, U. Stierlin and P. Weilhammer, Study of the dipion system, Proc. 1st EPS Conf. on meson resonances and related electromagnetic phenomena, Bologna, 1971, ed. R.H. Dalitz and A. Zichichi (Editrice Compositori, Bologna, 1972). p. 25 and 445.

[3] G. Grayer, B. Hyams, C. Jones, P. Schlein, W. Blum, H. Dietl, W. Koch, E. Lorenz, G. Lütjens, W. Männer, J. Meissburger, W. Ochs, U. Stierlin and P. Weilhammer, Phys. Letters 35B (1971) 610.

[4] G. Grayer, B. Hyams, C. Jones, P. Schlein, W. Blum, H. Dietl, W. Koch, E. Lorenz, G. Lütjens, W. Männer, J. Meissburger, W. Ochs, U. Stierlin and P. Weilhammer, Proc. 3rd Philadelphia Conf. on experimental meson spectroscopy, Philadelphia, 1972 (American Institute of Physics, New York, 1972) p. 5.

[5] G. Grayer, B. Hyams, C. Jones, P. Schlein, W. Blum, H. Dietl, W. Koch, E. Lorenz, G. Lütjens, W. Männer, J. Meissburger, W. Ochs, U. Stierlin and P. Weilhammer, Proc. 4th Int. Conf. on high-energy collisions, Oxford, 1972 (Rutherford High-Energy Laboratory, Didcot, Berks., 1972) vol. 2, p. 26.

[6] G. Grayer, B. Hyams, C. Jones, P. Schlein, P. Weilhammer, W. Blum, H. Dietl, W. Koch, E. Lorenz, G. Lütjens, W. Männer, J. Meissburger, W. Ochs and U. Stierlin, Phys. Letters 39B (1972) 563.

[7] G. Grayer, B. Hyams, C. Jones, W. Blum, H. Dietl, W. Koch, E. Lorenz, G. Lütjens, W. Männer, J. Meissburger, U. Stierlin and P. Weilhammer, Nucl. Instr. 99 (1972) 579.

[8] G. Grayer, B. Hyams, C. Jones, P. Weilhammer, W. Blum, H. Dietl, W. Koch, E. Lorenz, G. Lütjens, W. Männer, J. Meissburger, W. Ochs and U. Stierlin, Nucl. Phys. B50 (1972) 29.

[9] G. Grayer, B. Hyams, C. Jones, P. Schlein, P. Weilhammer, W. Blum, H. Dietl, W. Koch, E. Lorenz, G. Lütjens, W. Männer, J. Meissburger, W. Ochs and U. Stierlin, Paper No. 768 Contributed to the 16th Int. Conf. on high-energy physics, Batavia, 1972.

[10] B. Hyams, C. Jones, P. Weilhammer, W. Blum, H. Dietl, G. Grayer, W. Koch, E. Lorenz, G. Lütjens, W. Männer, J. Meissburger, W. Ochs, U. Stierlin and F. Wagner, Nucl. Phys. B64 (1973) 134.

[11] W. Hoogland, G. Grayer, B. Hyams, C. Jones, P. Weilhammer, W. Blum, H. Dietl, W. Koch, E. Lorenz, G. Lütjens, W. Männer, J. Meissburger and U. Stierlin, Isospin-2 $\pi\pi$ phase shifts from an experiment $\pi^+ p \to \pi^+ \pi^+ n$ at 12.5 GeV/c, submitted to Nucl. Phys.

[12] G. Grayer, B. Hyams, C. Jones, P. Schlein, P. Weilhammer, W. Blum, H. Dietl, W. Koch, E. Lorenz, G. Lütjens, W. Männer, J. Meissburger, W. Ochs and U. Stierlin, AIP Conf. Proc. 13 (1973) 117.

[13] P. Estabrooks, A.D. Martin, G. Grayer, B. Hyams, C. Jones, P. Weilhammer, W. Blum, H. Dietl, W. Koch, E. Lorenz, G. Lütjens, W. Männer, J. Meissburger and U. Stierlin, AIP Conf. Proc. 13 (1973) 37.

[14] Aachen-Birmingham-Bonn-Hamburg-London (I.C.)-Munich: L. Bondar, K. Bongartz, M. Deutschmann, E. Keppel, G. Kraus, H. Weberg, D.C. Colley, W.P. Dodd, J. Simmons, B. Tallini, A.M. Freine-Endler, B. Nellen, G. Winter, D. Cerds, Ch. Dehne, E. Lohrmann, P. Söding, M. Tencher, G. Wolf, J.M. Brownlee, I. Butterworth, F.I. Campayne, M. Ibbotson, N.N. Biswas, I. Derado, K. Gottstein, D. Lüers, G. Lütjens and N. Schmitz, Nuovo Cimento 31 (1964) 729.
[15] B. Hyams, W. Koch, D.C. Potter, J. Wilson, L. von Lindern, E. Lorenz, G. Lütjens, U. Stierlin and P. Weilhammer, Nucl. Phys. B7 (1968) 1.
[16] F. Bulos, R.K. Carnegie, G.E. Fischer, E.E. Kluge, D.W.G.S. Leith, H.L. Lynch, B. Katcliff, B. Richter, H.H. Williams, S.H. Williams and M. Beniston, Phys. Rev. Letters 26 (1971) 1453.
[17] D. Morgan, Rutherford High-Energy Lab. preprint RPP/T/27 (1972); J.L. Petersen, Phys. Reports 2 (1971) 155.
[18] E. Braunersreuter, CERN Internal report MSC/PR/689 (April, 1970).
[19] K. Boesebeck, H. Grässler, G. Kraus, R. Schulte, H. Böttcher, J. Kaltwasser, H. Kaufmann, S. Nowak, K. Böckmann, J.G. Bossen, H. Drevermann, W. Johnssen, M. Rost, K. Sternberger, U. Stöcker, A. Angelopoulos, J.R. Campbell, V.T. Cocconi, J.D. Hansen, W. Kittel, S. Matsumoto, D.R.O. Morrison, R. Stroynowski, J.B. Whittaker and J. Łoskiewicz, Nucl. Phys. B28 (1971) 381.
[20] K. Boesebeck, M. Deutschmann, H. Grässler, R. Honecker, G. Kraus, P. Kostka, H. Nowak, C. Spiering, J.G. Bossen, H. Drevermann, Ch. Kanazirsky, W. Johnssen, M. Rost, T. Besliu, K. Böckmann, V.T. Cocconi, P. Duinker, W. Kittel, D.R.O. Morrison, H. Schiller, W.J. Scott and J.B. Whittaker, Nucl. Phys. B40 (1972) 39.
[21] G.H. Trilling, Some topics in boson spectroscopy, LBL-351 preprint (1971).
[22] M.H. MacGregor, Nuovo Cimento 18A (1973) 169.
[23] Particle Data Group, Rev. Mod. Phys. 43 (1970) 2.
[24] Particle Data Group, Phys. Letters 39B (1972) 1.
[25] P. Estabrooks, B. Hyams, C. Jones, A. Martin, P. Weilhammer, W. Blum, H. Dietl, G. Grayer, W. Koch, E. Lorenz, G. Lütjens, W. Männer, J. Meissburger and U. Stierlin, ρ-ω interference in $\pi^- p \to \pi^-\pi^+ n$ at 17.2 GeV/c, to be published.
[26] M. Alston-Garnjost, A. Barbaro-Galtieri, S.M. Flatté, J.H. Friedman, G.R. Lynch, S.D. Protopopescu, M.S. Rabin and F.T. Solmitz, Phys. Letters 36B (1971) 152.
[27] S.M. Flatté, M. Alston-Garnjost, A. Barbaro-Galtieri, J.H. Friedman, G.R. Lynch, S.D. Protopopescu, M.S. Rabin and F.T. Solmitz, Phys. Letters 38B (1972) 232.
[28] S.D. Protopopescu, M. Alston-Garnjost, A. Barbaro-Galtieri, S.M. Flatté, J.H. Friedman, T.A. Lasinski, G.R. Lynch, M.S. Rabin and F.T. Solmitz, Phys. Rev. D7 (1973) 1279.
[29] R. Odorico, Phys. Letters 38B (1972) 37, 411.
[30] P.E. Schlein, Phys. Rev. Letters 19 (1967) 1052.
[31] E. Malamud and P.E. Schlein, Phys. Rev. Letters 19 (1967) 1056.
[32] W. Ochs and F. Wagner, Phys. Letters 44B (1973) 271.
[33] P.K. Williams, Phys. Rev. D1, (1970) 1312; G.C. Fox, Phenomenology in particle physics (Cal. Inst. Tech., Pasadena, 1971).
[34] J.P. Ader, M. Capdeville, G. Cohen-Tannoudji and Ph. Salin, Nuovo Cimento A56 (1968) 952.
[35] P. Baillon, F. Bulos, R.K. Carnegie, G.E. Fischer, E.E. Kluge, D.W.G.S. Leith, H.L. Lynch, B. Ratcliff, B. Richter, H.H. Williams and S.H. Williams, Phys. Letters 35B (1971) 453.
[36] P. Estabrooks, A.D. Martin, G. Grayer, B. Hyams, C. Jones, P. Weilhammer, W. Blum, H. Dietl, W. Koch, E. Lorenz, G. Lütjens, W. Männer, J. Meissburger and U. Stierlin, $\pi\pi$ phase shift analysis, CERN preprint TH-1661 (1973).

[37] G. Grayer, B. Hyams, C. Jones, P. Weilhammer, W. Blum, H. Dietl, W. Koch, E. Lorenz, G. Lütjens, W. Männer, J. Meissburger, W. Ochs and U. Stierlin, Resonance parameters for the ρ, f and g mesons, to be published.
[38] J. Pisùt and M. Roos, Nucl. Phys. B6 (1968) 325.
[39] F. von Hippel and C. Quigg, Phys. Rev. D5 (1972) 624;
J. Blatt and V. Weiskopf, Theoretical nuclear physics (Wiley, 1952) p. 359.
[40] J.A.J. Matthews, J.D. Prentice, T.S. Yoon, J.T. Carroll, M.W. Firebaugh and W.D. Walker, Nucl. Phys. B33 (1971) 1.
[41] C.D. Froggat and D. Morgan, Phys. Rev. 187 (1969) 2044.
[42] W.D. Appel, J.S. Ausländer, H. Müller, G. Sigurdsson, H.M. Staudenmaier, U. Stier, E. Bertolucci, I. Manelli, G. Perazzini, P. Rehak, A. Scribano, F. Sergiampietri and M.L. Vincelli, Phys. Letters 41B (1972) 542.
[43] P. Estabrooks and A.D. Martin, Phys. Letters 41B (1972) 350.
[44] J.V. Beaupré, M. Deutschmann, H. Graessler, P. Schmitz, R. Speth, H. Boettcher, J. Kaltwasser, H. Kaufmann, S. Nowak, A. Angelopoulos, K.W.J. Barnham, J.R. Campbell, V.T. Cocconi, P.F. Dalpiaz, J.D. Hansen, G. Kellner, W. Kittel and D.R.O. Morrison, Nucl. Phys. B28 (1971) 77.
[45] J.T. Carroll, R.N. Diamond, M.W. Firebaugh, W.D. Walker, J.A.J. Matthews, J.D. Prentice and T.S. Yoon, Phys. Rev. Letters 28 (1972) 318.